

<https://doi.org/10.1038/s43247-025-03128-w>

Signatures of widespread Surtseyan volcanism at the northern Reykjanes ridge

Check for updates

Jonas Preine ^{1,2}✉, Christian Hübscher ¹, Dominik Pałgan ³, Froukje M. van der Zwan⁴, Carina Dittmers¹, Annalena Friedrich¹, Sarah Beeth⁵, Vanessa Ehli^{1,6}, Jonathan Ford ^{1,6}, Benedikt Haimerl ¹, Lisa Ischebeck¹, Max Lackner¹, Maryse Schmidt¹, Jan Oliver Eisermann^{7,8}, Linus Budke ⁹, David Þór Óðinsson¹⁰, Kurt Panter ¹¹, Morgane Le Saout¹² & Nico Augustin ^{13,14}

Submarine explosive volcanism shapes seafloor morphology, impacts marine ecosystems, and poses risks to maritime infrastructure and coastal communities. However, its occurrences and drivers remain poorly constrained, especially for basaltic systems. Here we present evidence for widespread phreatomagmatic volcanism at the Reykjanes Ridge north of ~63.2°N, derived from high-resolution seismic reflection profiles, multibeam bathymetry, and seafloor imagery. Our data indicate a first-order depth control on eruption style: effusive volcanism dominates below ~300 m, producing hummocky edifices with strong seismic attenuation, whereas shallower depths favour Surtseyan eruptions, forming smooth volcanic cones with flanks comprising stratified, outward-dipping seismic reflections. When eruptions occur close to the water–air interface, flat-topped volcanoes form, some emerging as ephemeral islands before being submerged by storm wave base erosion. Our results show that Surtseyan eruptions have been a dominant and recurrent process along the Reykjanes Ridge north of ~63.2°N since the Last Glacial Maximum.

Most of Earth's volcanic activity occurs beneath the ocean surface, primarily along mid-ocean ridges, where continuous magmatic accretion builds new oceanic crust¹. Mid-ocean ridge volcanism is normally mafic and typically occurs as effusive eruptions, generating pillow, lobate and sheet flow lavas. While recent studies have revealed seafloor evidence for explosive volcanic activity at mid-ocean ridges, including volatile-driven fragmentation², deep explosion craters and fragmented deposits at ~4000 m water depth³, constructional Strombolian and volcanoclastic deposits⁴, and crater-forming eruptions along sediment-covered spreading axes⁵, the inaccessibility of submarine volcanoes limits direct observations, leaving critical gaps in our understanding of the mechanisms, frequency, and spatial distribution of these eruptions. These uncertainties are essential in shallow submarine environments, where interactions between magma and seawater can drive explosive eruptions that may

be associated with hazards to marine infrastructure and coastal communities.

One of the best-observed examples of such shallow-water mafic explosive activity along a hotspot-influenced mid-ocean ridge is the 1963 eruption of Surtsey⁶ (south of Iceland; orange star in Fig. 1a). Considered the type-example of basaltic phreatomagmatic submarine eruptions, this eruption coined the widely used term Surtseyan eruptions. The submarine eruption started 12 November 1963 at 130 m below sea level, with phreatomagmatic explosions along a 300–400 m long fissure that produced ash plumes and fragmented tephra deposits^{6,7}, building a tephra cone that breached the sea surface on 15 November 1963. Over its 3.5-year history, the eruption alternated between phreatomagmatic and effusive phases^{7,8}, with effusive lava flows armouring parts of the cone against marine erosion. At its peak, Surtsey reached 175 m above sea level and a bulk eruptive volume of

¹Institute of Geophysics, University of Hamburg, Hamburg, Germany. ²Department of Geology and Geophysics, Woods Hole Oceanographic Institution, Woods Hole, MA, USA. ³Department of Geophysics, University of Gdansk, Gdynia, Poland. ⁴Department of Physical Science and Engineering, King Abdullah University for Science and Technology (KAUST), Thuwal, Saudi Arabia. ⁵College of Earth, Ocean, and Atmospheric Sciences, Oregon State University, Corvallis, OR, USA.

⁶National Institute for Oceanography and Applied Geophysics–OGS, Sgonico (TS), Italy. ⁷Institute of Geosciences, Marine Geophysics and Hydroacoustics, Kiel University, Kiel, Germany. ⁸Center for Ocean and Society, Kiel University, Kiel, Germany. ⁹Senckenberg Research Institute and Natural History Museum, Frankfurt am Main, Germany. ¹⁰Marine and Freshwater Research Institute, Hafnarfjörður, Iceland. ¹¹Bowling Green State University, School of Earth, Environment and Society, Bowling Green, OH, USA. ¹²Department of Earth Sciences, University of Bergen, Bergen, Norway. ¹³GEOMAR Helmholtz Centre for Ocean Research Kiel, Kiel, Germany. ¹⁴OceanQuest Foundation to Support International Deep Ocean Discovery, KAUST, Thuwal, Saudi Arabia.

✉ e-mail: jonas.preine@uni-hamburg.de

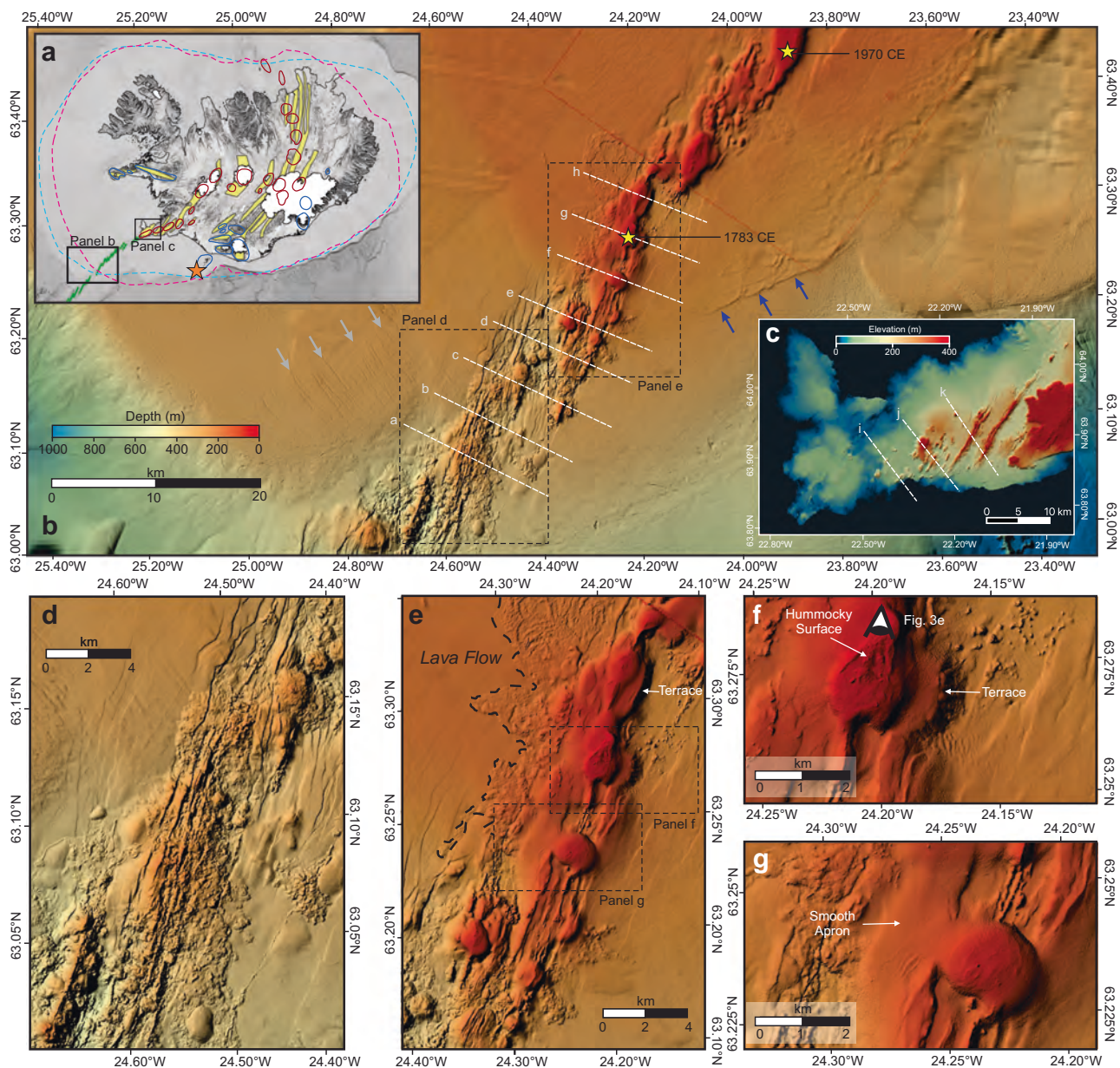


Fig. 1 | Morphology of the Northern Reykjanes Ridge. **a** Regional map of Iceland. Yellow areas mark fissure swarms; red circles mark central volcanoes of rift zones; blue circles mark volcanic flank zones; dashed lines mark the glacier extent during the Last Glacial Maximum inferred from 3D thermomechanical modelling (purple¹⁷) or empirical (blue¹⁸) green lines mark axial volcanic ridges (AVRs) along the Reykjanes Ridge; orange star marks the location of Surtsey and Surtla. Black boxes indicate the location of the study area and Reykjanes Peninsula. **b** Morphological map of the study area. Yellow stars mark historical eruption sites^{14,15}. Blue arrows indicate a braided system of moraines while grey arrows highlight erosional channels engrained in the sedimented terrain¹⁵. White dashed

lines indicate locations of bathymetric profiles shown in Fig. 2a–h. **c** Morphological map of the Reykjanes Peninsula. White dashed lines indicate locations of bathymetric profiles shown in Fig. 2i–k. **d** Enlargement of a section of the Reykjanes Ridge axis south of ~63.2°N characterized by a hummocky terrain with en-echelon fault patterns. **(e)** Enlargement of a section of the Reykjanes Ridge axis north of ~63.2°N characterized by a smooth topography. Black dashed lines indicate outline of a potential lava flow¹⁵. Locations of **(d, e)** are marked by the black boxes in **(c)**. **f, g** Enlargements of two smooth-shaped volcanic edifices north of ~63.2°N. Locations are marked by boxes in **(e)**. Eye-symbol **(f)** marks location of OFOS imagery shown in Fig. 3e.

~1.1 km³. The Surtsey eruptions occurred as part of a broader eruptive complex that produced three satellite edifices: Surtla, a submarine ridge ~2 km ENE of Surtsey (December 1963–January 1964); Syrtlingur, a small island 0.6 km ENE of Surtsey (May–October 1965); and Jólnir, a larger tuff cone ~1 km SW of Surtsey (December 1965–August 1966)⁶. Syrtlingur and Jólnir briefly emerged as islands up to 70 m high, but were destroyed by wave action within weeks of eruptive cessation, leaving only submarine flat-topped remnants^{6,9}. Geochemical and geophysical studies suggest that the feeder system tapped heterogeneous magmas emplaced at a propagating rift at the southern tip of the Vestmannaeyjar archipelago, mixing melts of

slightly different compositions and volatile contents, with Surtsey magmas containing higher H₂O (~0.5–1.0 wt%) and CO₂ (up to ~300 ppm)^{8,10} than typical mid-ocean ridge basalts from the southern Iceland (generally ~0.1–0.3 wt% H₂O, ~50–150 ppm CO₂)^{11–13}.

The Reykjanes Ridge, an oblique segment of the Northern Mid-Atlantic Ridge, represents a natural laboratory for studying shallow phreatomagmatic and potentially explosive volcanism (Fig. 1a, b). It extends approximately 900 km across the Northern Atlantic Ocean, between Iceland and the Bight Fracture Zone (57°N), making it the longest hotspot-influenced ridge globally. Its depth varies markedly, rising from about 2,600

meters depth near the Bight Fracture Zone to above sea level at the Reykjanes Peninsula (Fig. 1c). This makes it one of the few mid-ocean ridges that reaches land, offering the unique possibility to study submarine volcanism across a wide depth gradient (Supplementary Fig. S1). South of $\sim 59^\circ\text{N}$, the ridge is characterized by a distinct axial valley typical of slow-spreading ridges, whereas north of 63°N , the ridge axis transitions into a prominent axial high, resembling features found at fast-spreading ridges^{14,15} (Fig. 1b). The axial zone of the Reykjanes Ridge is marked by en-echelon axial volcanic ridges, which trend approximately 15° oblique to the overall orientation of the ridge (Fig. 1a, b). During the Last Glacial Maximum, extensive grounded ice sheets covered the Reykjanes Ridge as far south as $\sim 63.2^\circ\text{N}$ (red and blue dashed lines in Fig. 1a)^{16–18}. Evidence of the extent of the grounded ice sheets is preserved on the seafloor by braided systems of moraines and erosional channels¹⁵ (blue arrows and grey in Fig. 1b).

Recovered lithologies from the ridge include picrite basalts, olivine tholeiites and tholeiites, which are broadly characteristic of basaltic magmatism along the hotspot-influenced Reykjanes Ridge and consistent with those reported from the dominantly effusive volcanism on the western Reykjanes Peninsula^{19–21} (Fig. 1c). Historical records document at least 14 eruptions along the northern Reykjanes Ridge over the past 1000 years¹⁴ (yellow stars in Fig. 1b), including the brief emergence of Nýey island in 1783 that was eroded and submerged within few months. Apart from these historical accounts, our knowledge about the formation mechanisms, processes and lithologies of submarine volcanoes at the Northern Reykjanes Ridge remains poorly constrained.

In this study, we present high-resolution seismic data from Expedition M201 that image the shallow structure of the Northern Reykjanes Ridge²² (Fig. 1b). The primary objectives of this study are to (i) characterize the morphology and internal architecture of submarine volcanoes along the Northern Reykjanes Ridge, (ii) investigate probable formation mechanisms of these volcanic edifices, and (iii) relate the morphology of the volcanoes to their eruption depths.

Results

Morphology of the Northern Reykjanes Ridge

The volcanic edifices along the Reykjanes Ridge rift axis display distinct topographical variability, with a marked morphological boundary occurring at $\sim 63.2^\circ\text{N}$ (Figs. 1b, d, e and 2a–h, Supplementary Fig. S1). A transition from high to low roughness is evident in representative topographic profiles across the Northern Reykjanes Ridge (Fig. 2a–h). We use these profiles to calculate a relative composite roughness index based on the normalized standard deviation of slope along each profile (Fig. 2l), a metric that emphasizes relatively large-scale (> 20 m) morphological variability^{23,24}. In addition, we calculate the relative roughness from 33 profiles perpendicular to the ridge axis (Supplementary Table 1; Supplementary Fig. S2). South of $\sim 63.2^\circ\text{N}$, the ridge is characterized by rugged, uneven terrain, where volcanic ridges and cones exhibit hummocky morphologies and abundant surface faulting, typical of mid-ocean ridges worldwide²⁵ (Figs. 1d and 2a–d, Supplementary Fig. S3). Relative roughness values in this region are high (average of 0.16 ± 0.01 ; Fig. 2l), comparable to profiles measured onshore the western Reykjanes Peninsula, which is characterized by faulting, lava flows, and volcanic edifices predominantly formed by effusive basaltic eruptions²⁶ (Figs. 1c and 2i–k). There, the average relative roughness value is 0.17 ± 0.01 (Fig. 2l).

In contrast, north of $\sim 63.2^\circ\text{N}$, the ridge becomes shallower (< 300 m) and noticeably smoother (average relative roughness: 0.06 ± 0.004) (Figs. 1e and 2f–h). Several of these smooth volcanic structures exhibit terraces along their flanks (Figs. 1f and 2g, h). We calculate relative roughness only up to $\sim 63.33^\circ\text{N}$, beyond which no high-resolution bathymetric data are available (Fig. 2l). Nevertheless, lower-resolution GEBCO bathymetry beyond this latitude suggests that the smooth morphological character continues further north along the Reykjanes Ridge (Supplementary Fig. S1). A representative profile across the morphological transition at $\sim 63.2^\circ\text{N}$ (Fig. 2e) shows intermediate relative roughness (0.12 ± 0.01) (Fig. 2l).

Morphometric analysis further underscores this transition. Volcanic edifices north of $\sim 63.2^\circ\text{N}$ exhibit characteristically low height-to-width (H/W) ratios when compared to 571 submarine effusive volcanoes between $\sim 63.2^\circ\text{N}$ and $\sim 57.83^\circ\text{N}$ (Fig. 2m)²⁷. Using a previously published classification scheme²⁷ and incorporating morphometric zones defined for flat-topped and shield volcanoes^{28,29}, we show that the volcanoes in our study area fall within a transition zone between these two types (Fig. 2m). Despite increasing widths, their heights remain below 300 m, forming a morphological plateau (Fig. 2m). The average H/W ratio is ~ 0.07 , notably lower than the ~ 0.13 H/W average observed farther south along the Reykjanes Ridge²⁷, and more comparable to the submarine Surtseyan edifices Syrtlingur (H/W ~ 0.09), Jólnir (H/W ~ 0.07), and Surtla (H/W ~ 0.12)⁹, as well as the Surtseyan-type volcano Black Point in the Mono Craters volcanic system (H/W ~ 0.1)³⁰.

Seismic imaging of the Northern Reykjanes Ridge

Three representative seismic profiles across the Reykjanes Ridge give insights in the internal architecture of the different morphologies (Fig. 3). The seismic profile in Fig. 3b spans two axial volcanic ridges separated by an approx. 3.5 km wide valley south of $\sim 63.2^\circ\text{N}$. Distal from the ridge axis, the seafloor is flat, where we identify weakly reflective, stratified sediments in our section, cut and offset by faults, some of which reach the seafloor (Fig. 3b). The max. 170 m thick (assuming an internal P-wave velocity of 1700 m/s) sediments overlie an acoustic basement (black dotted lines, Fig. 3b) and within the sediments, a distinct unconformity can be identified (orange dotted lines, Fig. 3b). The western axial volcanic ridge is characterized by hummocky terrain at the seafloor and acoustic blanking below it (Fig. 3b). At the western shoulder of the valley, we identify a ~ 2 km wide volcanic edifice with a hummocky surface and no internal reflections (Fig. 3b). The valley itself shows several faults and some faint, westward-dipping reflections (Fig. 3b). East of the valley, we identify a faulted volcanic edifice with some internal reflections visible (Fig. 3b). The eastern margin of the Reykjanes Ridge is marked by a smaller volcanic cone with steep, smooth flanks and low-amplitude internal reflections forming internal stratification (Fig. 3b).

The seismic profiles in Fig. 3c, d cross the ridge axis north of $\sim 63.2^\circ\text{N}$. Both profiles cross distinct volcanoes at the center of the ridge axis that are characterized by smooth flanks (Fig. 3c, d). Off-axis, we identify sediments showing stratified, low-amplitude reflections reaching a maximum thickness of about 250 m (Fig. 3c, d). Similar to the seismic profile in Fig. 3b, they are separated by a high-amplitude reflection with a hummocky topography (orange dotted lines, Fig. 3c, d), and are cut by several faults. Closer to the ridge axis, the sediments lose visibility beneath volcanic edifices that cause acoustic blanking (Fig. 3c, d). The cone crossed by the seismic profile in Fig. 3c has a flat top and shows low-amplitude, outward-dipping reflections at its center. We observe several internal unconformities within the edifice (red dotted lines, Fig. 3c) and faults. The flanks of this cone comprise stratified reflections with low amplitudes that can be traced away from the volcanic edifices, dipping at angles of $\sim 17^\circ$. On the eastern flank, overlying the unconformity marked by the orange dashed line, the apron of the edifice is characterized weak, stratified reflections that can be traced for more than 6 km (Fig. 3c). The western side of the edifice is characterized by a volcanic cone adjacent to a hummocky terrain, associated with pronounced acoustic blanking underneath that corresponds to a lava flow visible in bathymetry¹⁵ (Fig. 3c).

The seismic profile in Fig. 3d shows a flat-topped volcano with a summit, characterized by an irregular central terrain (Fig. 3d). Ocean floor images acquired by the Ocean Floor Observation System (OFOS) across this hummocky terrain show the presence of large, rounded boulders and rounded rock fragments on top of cobbles (Fig. 3e and Supplementary Fig. S4). Underneath this hummocky terrain, we observe a laterally confined area of intense acoustic blanking and upwards-bent reflections. The flanks of this edifice are characterized by SE-ward dipping, low-amplitude reflections with dip angles of about $\sim 18^\circ$ (Fig. 3d). There are several internal unconformities within the edifice, with the upper one forming a terrace-like

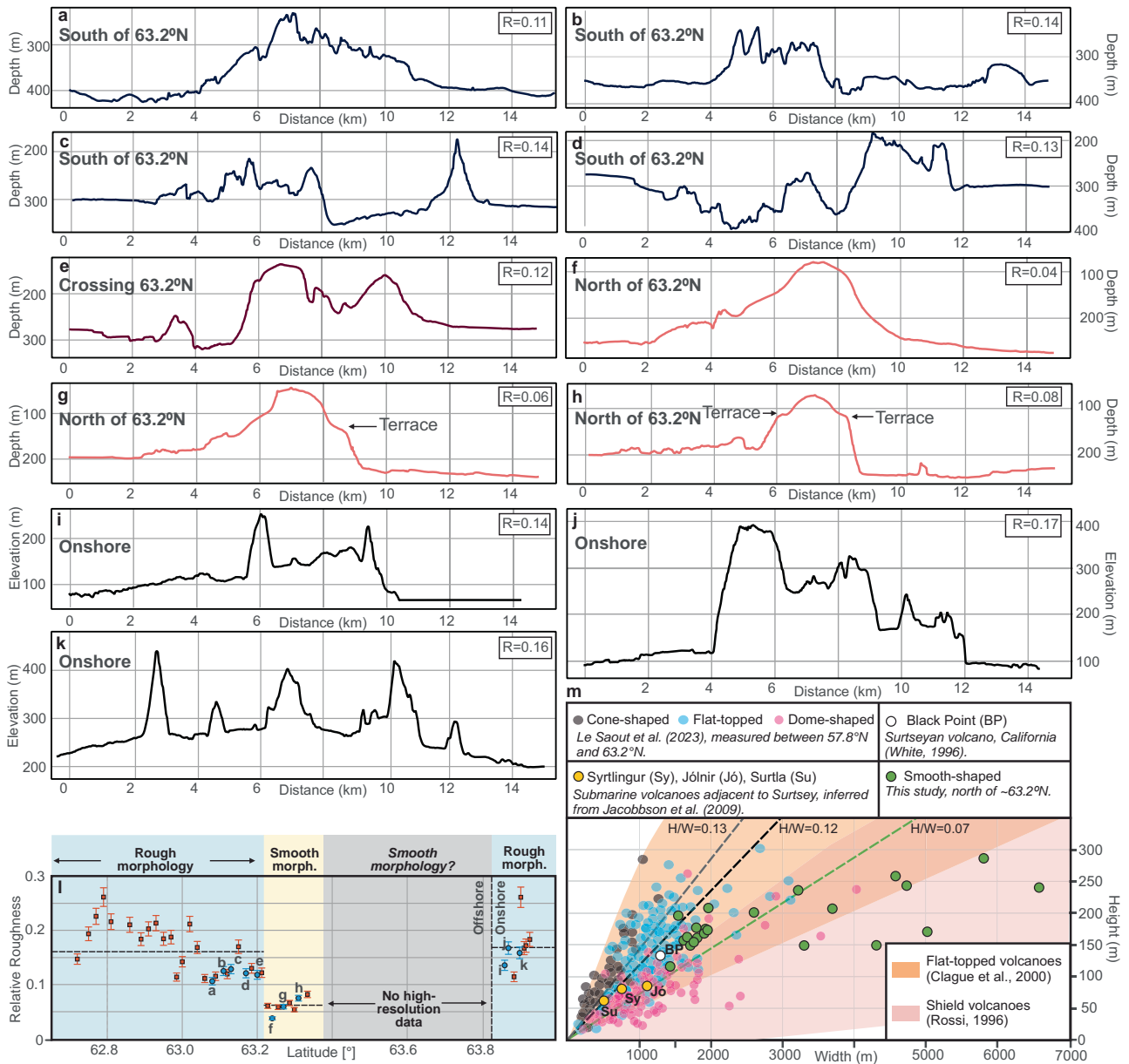


Fig. 2 | Edifice morphometric parameters. **a–h** Bathymetric profiles across the Northern Reykjanes Ridge. Profiles south of ~63.2°N are marked blue, profiles north of ~63.2°N are marked red. Location is shown in Fig. 1b. Direction of all profiles is NW–SE. R: Relative Roughness. (**i–k**) Topographic profiles across the Reykjanes Peninsula. Location is shown in Fig. 1c. **l** Morphometric variability along 44 topographic profiles across the Reykjanes Ridge and Reykjanes Peninsula. The scatter plot shows relative large-scale (> 20 m) surface roughness (defined as the standard deviation of slope) plotted against latitude. Profiles corresponding to (**a–k**) are highlighted in blue, while additional profiles are shown in orange. Error bars represent 99% confidence intervals derived from the slope variability within each profile. Semi-transparent shaded areas mark zones of interpreted relatively rough and smooth morphology. Dashed horizontal lines indicate average relative roughness values measured for these intervals. Latitude refers to the center point of each profile. All roughness values, coordinates, and associated uncertainties are

summarized in Supplementary Table S1. The full set of profile locations is shown in Supplementary Fig. S2. Selected profiles on a joint depth axis are shown in Supplementary Fig. S3. **m** Height versus width for submarine cones from the Reykjanes Ridge north of ~63.2°N (green; this study). Grey, blue and purple circles indicate volcanoes mapped and characterized between ~63.2°N and ~57.83°N²⁷. Orange circles indicate submarine volcanoes associated with the 1963 Surtsey eruption⁹. White circle indicates exposed Surtseyan Black Point volcano³⁰. Semi-transparent orange and pink areas indicate morphometric fields for effusive flat-topped²⁸ and shield volcanoes²⁹ for comparison²⁷. Dashed line indicate the average height-width ratios of volcanoes south of 63.2°N (0.13) and north of 63.2°N (0.07), as well as the height-width ratio (H/W) of 0.12, that has been proposed to distinguish explosive volcanism in deep-sea (> 0.12) and shallow water (< 0.12) with potential interaction of eruption columns with the sea surface⁸⁹.

outcrop at the flank (Fig. 3d). Similar to the seismic profile in Fig. 3c, this edifice forms a laterally extensive apron. The northwest flank of the edifice is characterized by irregular morphology atop acoustic blanked reflections, where a lava flow is visible in the bathymetry (Fig. 3c, d).

To enhance the visualization of the internal architecture of several volcanic edifices of the Reykjanes Ridge, we employ the instantaneous phase

seismic attribute (Fig. 4). This representation shows that the smooth-shaped volcanoes have a similar internal architecture (Fig. 4). In all profiles, we observe well-stratified, outward-dipping (~19–29°) reflections at the flanks and incoherent strata in the center (Fig. 4). The stratified reflections exhibit a pattern of growth, both in height and lateral extent, as they progress outward and downlap the underlying strata (yellow arrows, Fig. 4). At the volcanic

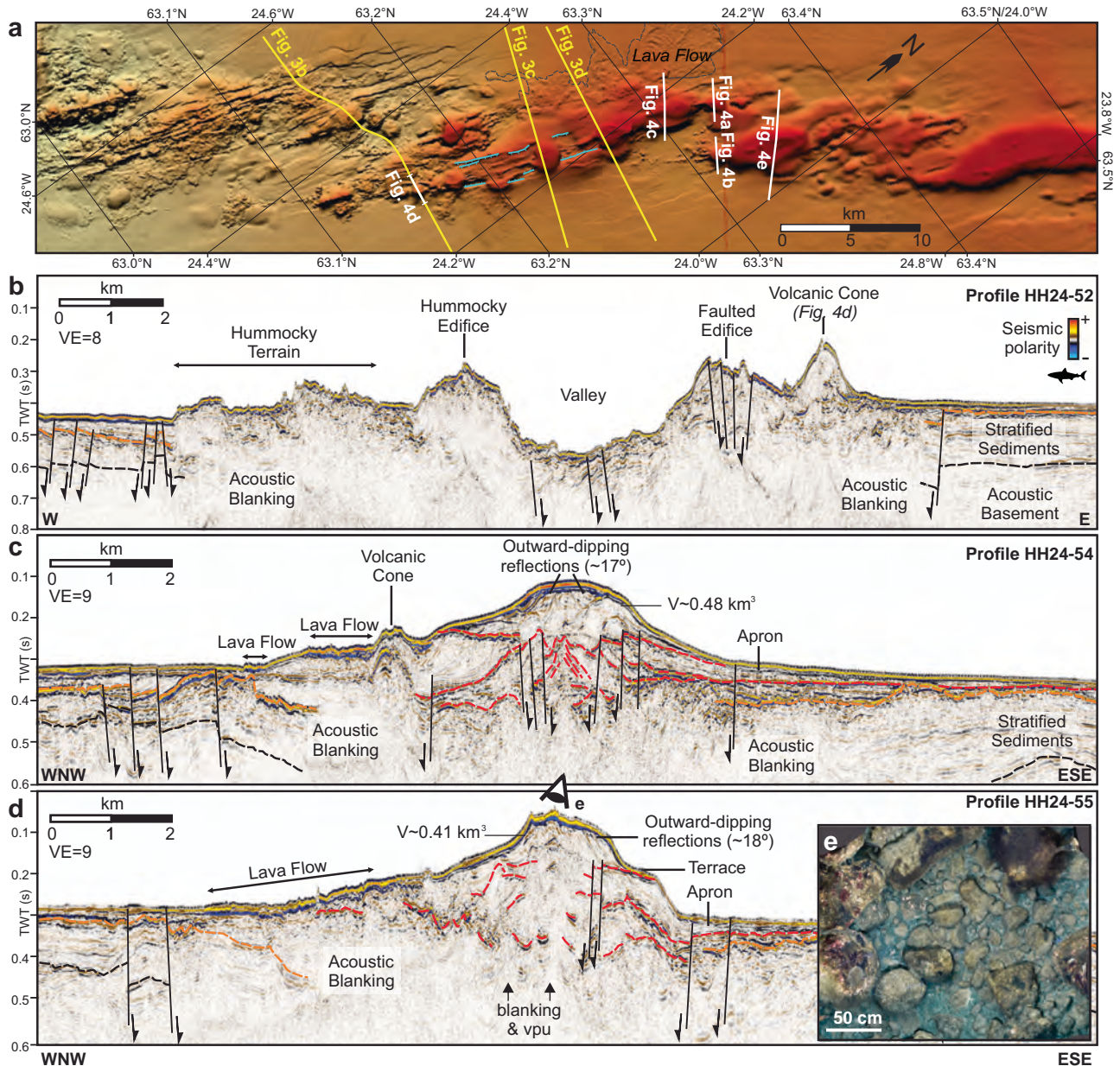


Fig. 3 | Seismic profiles crossing the Northern Reykjanes Ridge. a Rotated morphological map showing the location of seismic profiles shown in panels (b–d) (yellow lines) and Fig. 4a–e (white lines). Black dashed lines indicate the outline of a potential lava flow¹⁵. Light blue lines indicate faults¹⁵. **b** Seismic profile crossing the hummocky ridge axis south of ~63.2°N. **(c, d)** Seismic profiles crossing the smooth ridge axis north of ~63.2°N. Red dotted lines indicate internal unconformities and high-amplitude reflections within the edifice; orange dotted line indicates an unconformity within the sedimentary strata off-axis; black dotted lines indicate the top of the acoustic basement. VE: = Vertical Exaggeration. Vpu: velocity pull-up. V:

Estimated bulk volume (Supplementary Table S2, Supplementary Figures S6–S7). Uninterpreted versions are included in Supplementary Fig. S8 and profiles without vertical exaggeration are shown in Supplementary Fig. S9. **e** Block field of volcanic debris on top of the volcanic edifice crossed by the seismic profile in panel (d). 3D reconstruction of images acquired with the Ocean Floor Observatory System (OFOS). The approximate location of the OFOS image is indicated by eye-symbol and in Fig. 1f. An enlarged version of this 3D reconstruction is included in Supplementary Fig. S4.

edifices imaged in Fig. 4c, e, the flanks form aprons, that can be traced for several kilometers. At nearly all cones, internal reflections show toplap terminations (black arrows, Fig. 4a–c, e). For some cones, this termination is only discernible in the instantaneous phase plot, since the remnant of a seismic source bubble reflection masks the internal reflection configuration and introduces conflicting dips (grey circles in Fig. 4). Only at the edifice imaged in Fig. 4d do we observe no top-lap terminations. The internal reflections, instead, bend towards the center of the edifice with steeper dips of about 29°, where they lose coherency.

Several observed volcanoes exhibit a stacking behaviour where successive layers of stratified reflections are superimposed (Fig. 4c, e). Here, we

observe downlap/toplap terminations towards internal unconformities, which form terraces along the flanks of the edifices (Fig. 4c, e) that are also clearly expressed in the bathymetry (Figs. 1e and 2g, h). Most volcanoes have relatively smooth tops, but some have distinct small-scale positive structures, forming pinnacles at their center (Fig. 4b, d). The volcano imaged in Fig. 4b shows a distinct zone of high-amplitude reflections underneath its central peak. The volcanic edifice imaged in Fig. 4e is characterized by a complex internal architecture with several stacked, stratified low-amplitude reflections with top- and downlap terminations. The summit of this edifice is characterized by a hummocky, high-amplitude reflection, accompanied by strong acoustic blanking beneath it (Fig. 4e). At all investigated volcanoes,

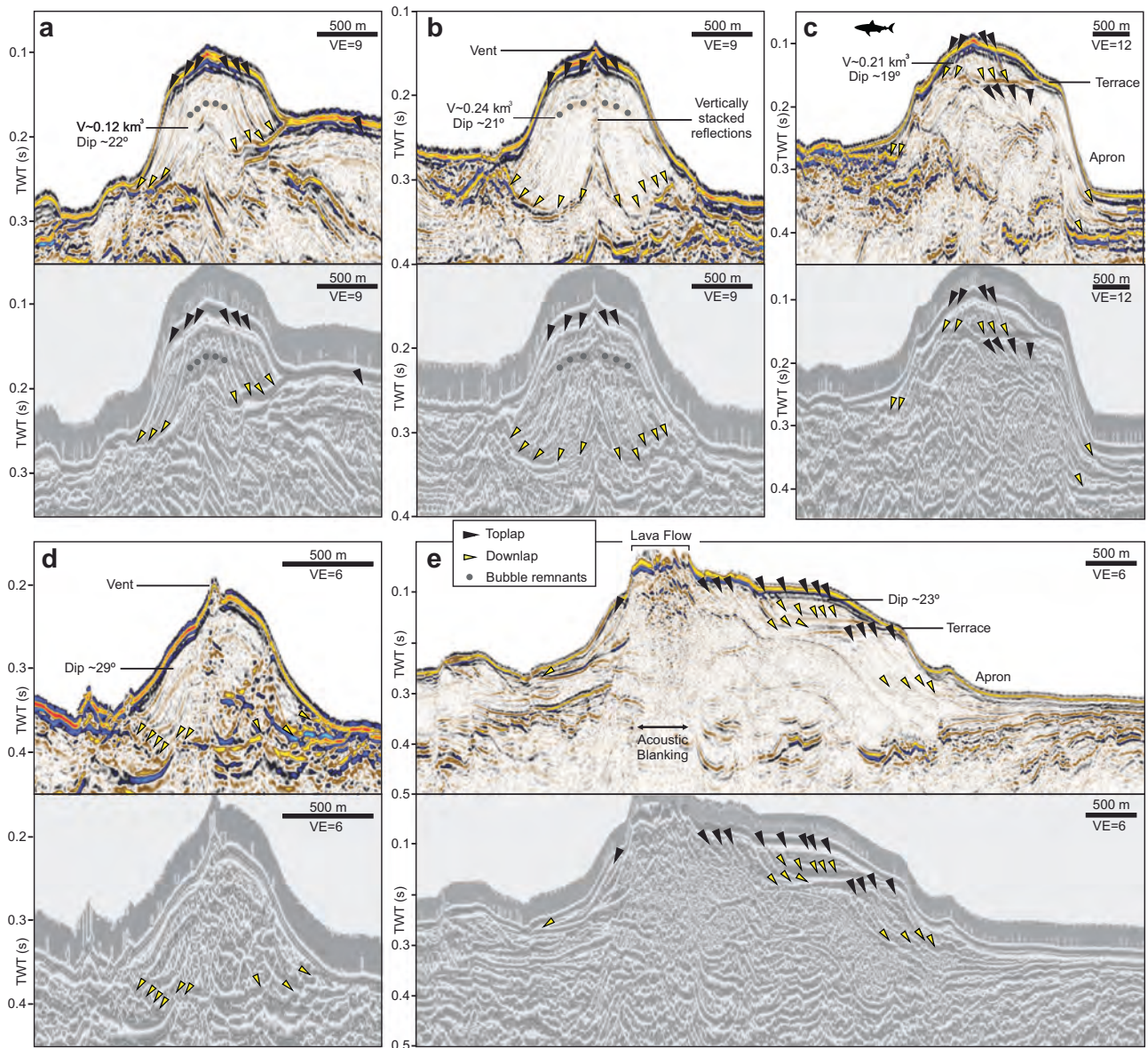


Fig. 4 | Internal architecture of volcanic edifices along the Northern Reykjanes Ridge. a–e Seismic profiles crossing volcanic cones at the Northern Reykjanes Ridge (upper panels) and their corresponding instantaneous phase attribute plots shown in grey-scale (lower panels). For locations see Fig. 3a. Uninterpreted versions are included in Supplementary Fig. S10. Versions without vertical

exaggerations are shown in Supplementary Fig. S11. VE = Vertical Exaggeration. V: Estimated bulk volume (Supplementary Table S1, Supplementary Figs. S6 and S7). Black arrows represent toplap; yellow arrows represent downlap. Grey circles indicate remnants of the bubble reflection.

we identify coherent reflections underneath the edifices. The underlying strata only become warped or blanked underneath the central parts of the volcanoes. This contrasts with the volcanic edifices imaged south of ~63.2°N (Fig. 3b), where no coherent reflections appear underneath the volcanoes, except for the small cone imaged in Fig. 4d.

Discussion

Internal architecture of the Northern Reykjanes Ridge

The presented seismic profiles reveal the internal architecture of the Reykjanes Ridge (Figs. 3, 5). Off-axis, a layered sedimentary sequence overlies an acoustic basement, interpreted as the rifted and subsided oceanic basement³¹ (Figs. 3 and 5). Within these strata, we identify a prominent unconformity characterized by a hummocky surface and local truncation of underlying reflectors (orange lines, Figs. 3 and 5c, d), which is a characteristic morphology of glacial erosion surfaces^{32,33}. This interpretation is consistent with the study area’s location within the estimated extent of grounded ice during

the Last Glacial Maximum around 20 ka^{17,18} (Fig. 1a and 5a, b) and by the observation that, away from the rift axis, the sediment cover above this unconformity thins considerably (Fig. 5c, d), particularly east of the ridge, where a system of braided moraines is visible on the seafloor¹⁵ (Fig. 1b and 5b). Seismic profiles show that the unconformity locally crops out at the seafloor, coinciding with areas of elevated reflection amplitudes (green arrows, Fig. 5b–d), that likely reflect strong impedance contrasts typical of glacial till, which generally comprises unsorted sediment mixtures of clay, silt, sand, gravel, and boulders^{33–35} (Supplementary Fig. S5). In contrast, the overlying deposits exhibit lower amplitudes, consistent with softer hemipelagic sediments possibly mixed with volcanoclastic material³⁶ (Fig. 5c, d).

Lava flows are known to cause strong attenuation of seismic energy due to the presence of layers with high impedance contrasts and scattering from rugose internal interfaces, causing an amplitude blanking effect that reduces the amplitude of underlying reflections^{37,38}. This explains the non-visibility

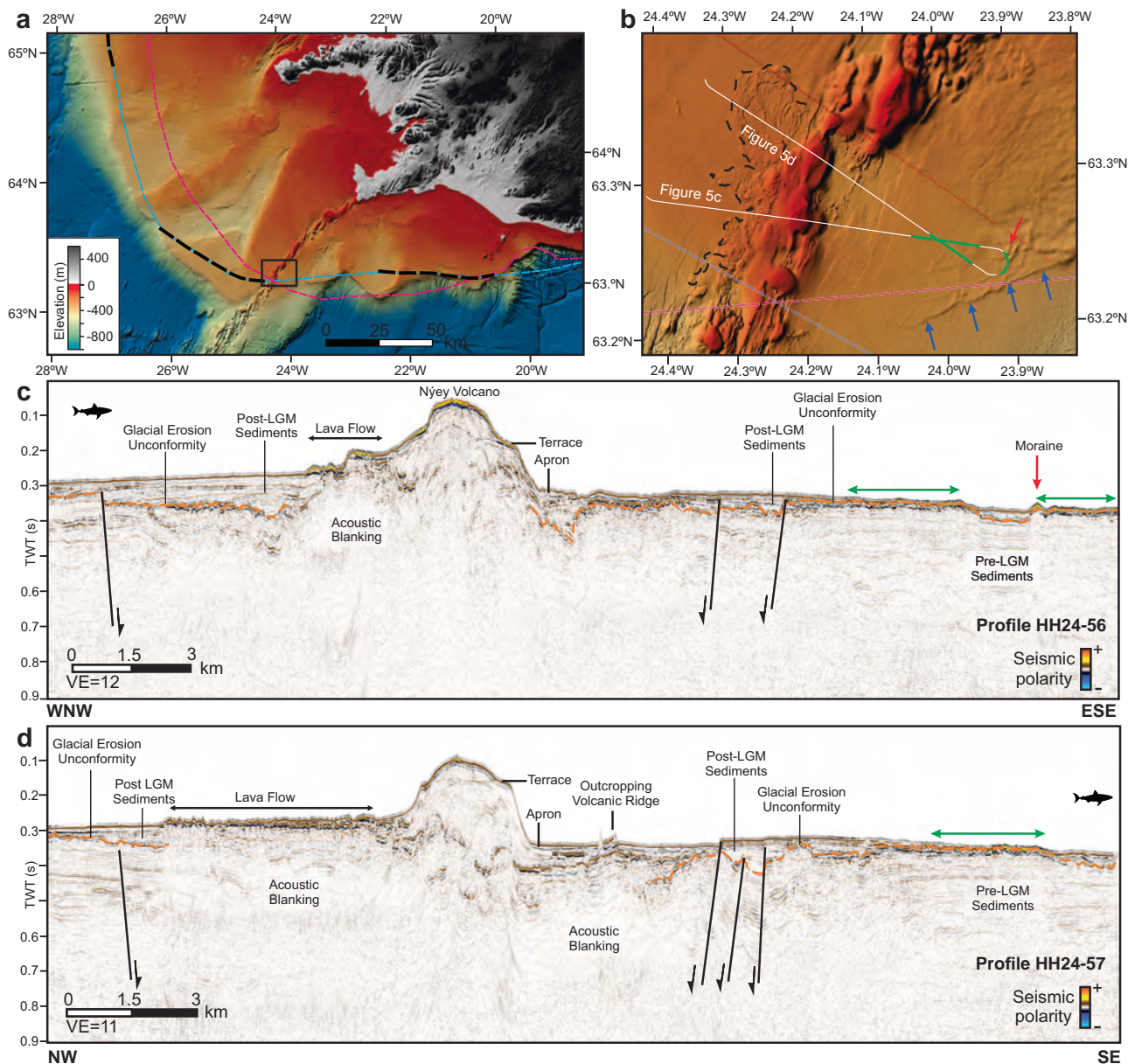


Fig. 5 | Geophysical signatures of the Last Glacial Maximum at the northern Reykjanes Ridge. **a** Regional map of western Iceland including the northern Reykjanes Ridge. Dashed lines mark the glacier extent during the last glacial maximum (LGM) at about 20 ka BP inferred from 3D thermomechanical modelling (purple¹⁸) or based on empirical data (blue and black) informed by moraines and other physical evidence^{19,99–103}. **b** Enlargement of the study area. Blue arrows mark the outer limit of a system of a braided system of moraines¹⁵, crossed by the seismic lines (white lines) shown in (c, d). **c, d** Interpreted seismic profiles crossing the northern Reykjanes

Ridge including the submerged volcano Nýey (c) and a prominent lava flow west of the ridge axis¹⁵ (d). The orange dotted line indicates the interpreted glacial erosion unconformity, cropping out at the seafloor where the bathymetry indicates glacial moraine complexes. Red arrow in (c) marks a ridge interpreted as a glacial moraine. Green arrows mark areas of high-reflection amplitudes at the seafloor, associated with a more hummocky seafloor marked in (b). Uninterpreted versions are included in Supplementary Fig. S5.

of sediments below the lava flows at the ridge axis (Figs. 3, 5). South of ~63.20°N, we observe no coherent reflections underneath the laterally extensive hummocky terrain and the hummocky edifice west of the valley (Fig. 3b), indeed indicating strongly attenuating lithologies. In contrast, the notably faulted edifice and the small cone east of the valley show some coherent reflections at their base, indicating less attenuating volcanic lithologies (Fig. 3b). The same applies to the smooth-shaped volcanoes north of ~63.2°N, where we identify several coherent internal reflections as well as a semi-continuous basal reflection (Fig. 3c, d). Most of these volcanoes display complex stacking behaviour indicated by the internal unconformities and terrace structures (Figs. 1f, 2g, h, 3c, d, 4c, e, 5c, d). While these

volcanic edifices show no faults at their surface, the seismic images provide evidence of internal faulting (Fig. 3c, d). Internal reflections within the volcano imaged in the seismic profile in Fig. 3c resemble the faulted edifice in Fig. 3b, suggesting that an earlier volcanic edifice was dissected by SW-NE rift-related faulting (light blue lines in bathymetry of Fig. 3a). The surface expression of these faults becomes muted where they are blanketed by upper volcanic edifice, which shows no evidence for rift-related deformation itself (Fig. 3c). This indicates a temporal hiatus between successive eruptive phases. Extensive lava flows, associated with a hummocky surface reflection and strong acoustic blanking beneath, are observed primarily on the western flank of the smooth-shaped volcanoes (Figs. 1e, 3c, d, 5c, d).

Effusive vs. explosive volcanism

Submarine eruptions are shaped by physical constraints fundamentally different from those for subaerial eruptions³⁹. These include the hydrostatic pressure, bulk modulus, thermal conductivity, heat capacity, density of the water mass compared to air, as well as magma–water interaction³⁹. Effusive submarine eruptions involve extrusion of lava, which is low in exsolved gas and rapidly forms a crust upon contact with cooling seawater, forming a range of morphologies, including pillow, lobate, and sheet flows. Explosive eruptions, in contrast, occur due to rapid gas expansion or interaction between magma and water, generating highly fragmented material that is subsequently emplaced as eruption-fed density currents and volcanoclastic turbidites^{39,40}. Theoretical models and numerical experiments demonstrate that explosive submarine eruptions of basalt are strongly influenced by water depth, volatile content, and the role of condensable vapour jets, which drive efficient fragmentation and dispersal of pyroclasts^{41–43}. Explosive submarine eruptions disperse material over large areas and can markedly reshape the seafloor^{43–45}. A transitional process between effusive and explosive volcanism occurs when lava comes into direct contact with water and shatters due to rapid cooling and quenching³⁹. This process forms hyaloclastites, composed of fine to coarse autoclastic glass fragments and breccias that accumulate in thick deposits⁴⁶. All of these eruption styles can generate volcanoclastic deposits, defined as sediments composed predominantly of volcanic fragments (> 25%), formed either primary, directly during eruption or secondary, through subsequent remobilization^{46,47}.

The hummocky, high-amplitude reflections with pronounced acoustic blanking underneath, e.g. in Figs. 3c and 5d and south of ~63.2°N (Figs. 1b, d and 2a–d, l), correspond to an extensive lava flow visible in the bathymetry (Figs. 1b, e, 3a, 5b). These acoustic features are typical for lava flows and effusive volcanism as recognized at other submarine volcanoes^{48,49}, implying that they are primarily formed by effusive eruptions, producing dense deposits of strongly attenuating lithologies⁴⁹, as would be expected for the Reykjanes Ridge given the mafic nature of the magmatism^{15,19–21,27}.

In contrast to the rugged, dome-shaped volcanoes south of ~63.2°N and onshore Reykjanes Peninsula, volcanic edifices north of this latitude share two defining features: (1) they exhibit markedly smoother topography draping the ridge axis (Figs. 1e–g, 2e–g, l), and (2) they consist of stratified, coherent, outward-dipping seismic reflections that form laterally extensive aprons (Figs. 3c, d, 4, 5c, d). Smooth volcanic flanks are a common observation at volcanoclastic aprons, where eruption-fed tephra and debris drape the underlying topography and mute small-scale relief⁵⁰. Conceptual facies models show that submarine volcanoclastic aprons consist of coarse breccias, lapilli tuffs, and ash that accumulate into laterally extensive, stratified aprons^{51,52}. Observations from active submarine volcanoes, such as NW Rota-1 in the Mariana Arc, demonstrate how eruption-fed plumes and pyroclastic density flows redistribute volcanoclastic material and create smooth draping deposits⁵³. In addition to direct eruptive deposition, mass-wasting processes can generate comparable aprons: flank collapses, debris avalanches, and subsequent sediment redistribution can equally blanket pre-existing topography^{54,55}.

Stratified, coherent, low- to medium-amplitude reflections within volcanic edifices have been consistently interpreted as volcanoclastic deposits, and this relationship is observed across a range of geological settings and magma compositions:

- Mafic systems: In the Faroe–Shetland Basin, hyaloclastite foresets at the front of lava deltas form medium-amplitude, prograding reflections that downlap onto the underlying substrate^{56,57}. Likewise, in the Azores, volcanic cones in the southeastern Terceira Rift display well-stratified internal reflections interpreted as volcanoclastic deposits, derived from mafic explosive eruptions, similar to those associated with onshore cinder cones⁵⁸.
- Intermediate to felsic systems: In the South Aegean, the submarine Kolumbo Volcanic Chain has been extensively covered by reflection seismic data, revealing low-amplitude stratified flanks^{59,60}, which correspond to layered volcanoclastic deposits drilled^{61,62} during IODP expedition 398 and imaged at the crater walls by ROV surveys⁶³.

Kameni Volcano within Santorini Caldera is largely composed by well-stratified deposits from the 726 CE eruption, contrasting strongly with subsequent lava flows, characterized by incoherent reflections and strong seismic attenuation⁴⁹. Similar seismic facies have been documented at buried monogenetic volcanoes in the Canterbury Basin (New Zealand)^{64,65} and the Bass Basin (Australia)⁴⁸, where drilling confirmed volcanoclastic compositions. On the Hikurangi Plateau, wedges of laminated reflectors interpreted as highly fragmented volcanoclastic deposits have been imaged around volcanic cones⁶⁶. In addition, stratified seismic flanks at Nisida Bank (Campi Flegrei) have been attributed to successive pyroclastic density currents⁶⁷.

Despite the diverse tectonic settings, magma chemistries, and eruption dynamics, all of these systems share one commonality: the production and submarine accumulation of volcanoclastic material. The produced material settles into stratified sequences if not remobilized by subsequent mass-wasting. In seismic reflection data, volcanoclastic deposits appear as coherent, low- to medium-amplitude reflections within the flanks or aprons of volcanic edifices^{49,56–59,62,64–67} (Figs. 3c, d, 4, 5c, d). In the distal region, volcanoclastic material can transition into turbidite currents, where it is deposited as fining-upward sequences expressed by inhomogeneous layers with incoherent, weak-amplitude internal reflections^{44,68}. Similar seismic characteristics are observed in deposits from volcanic flank collapses, which form acoustically chaotic or transparent sequences in distal settings⁶⁹. While collapse deposits may locally blanket flanks, they lack the well-ordered, outward-dipping stratification of proximal primary facies that typifies construction by repeated eruptive episodes^{69,70}.

The consistent occurrence of stratified, coherent, low- to medium-amplitude reflections across diverse settings suggests that constructional primary volcanoclastic deposits impart a characteristic proximal seismic signature in the submarine environment. To our knowledge, no comparable seismic facies have been documented for volcanic edifices built by predominantly effusive eruptions as these facies contrast the chaotic, high-amplitude, and rapidly attenuating internal reflections typical of effusive volcanic edifices, which are shaped by coherent lava accumulation rather than particulate dispersal⁴⁸. Thus, the presence of smooth topography and stratified reflections in seismic profiles of the volcanoes of the Reykjanes Ridge north of ~63.2°N indicates a dominance of primary volcanoclastic deposits within these edifices, pointing to explosive and/or hyaloclastic fragmentation processes.

Additional support for the presence of volcanoclastic deposits on the Northern Reykjanes Ridge comes from dredging studies that recovered layered hyaloclastite tuffs from several smooth-flanked edifices at the Northern Reykjanes Ridge²¹ (Supplementary Fig. S1). Although these particular volcanoes were not imaged in our seismic survey, their morphology closely resembles that of the edifices analysed in this study, being characterized by flat summits, low height-to-width ratios, and laterally extensive, gently sloping flanks (Supplementary Fig. S1). Given their consistent morphological expression and shared bathymetric setting, it is reasonable to infer that similar volcanic processes, including magma–water interaction and the deposition of volcanoclastic material, contributed to the construction of volcanic edifices north of ~63.2°N. Indeed, previous work²¹ concluded that the volcanic edifices between 63.18°N and 63.45°N consist of breccias, hyaloclastites, pillow lavas probably formed in submarine eruptions, and interpreted them as primarily constructional in origin.

However, it is important to note that, given the mafic composition, the location, and relatively modest sizes of the volcanoes north of ~63.2°N, the processes generating these volcanoclastic deposits differ in scale and impact from those observed at larger felsic systems, particularly those producing major pyroclastic density currents^{43,44}.

Surtseyan volcanism

Along the Reykjanes Ridge, basaltic magmas are prevalent¹⁹. Consequently, these magmas are less likely to have the viscosity and volatile content

required to drive highly explosive eruptions. Available, but sparse, geochemical datasets show broadly uniform MgO contents along the ridge axis, with only subtle increases in K_2O/TiO_2 ratios and radiogenic isotopes north of $\sim 60.5^\circ N$ but without a fundamental compositional break across $63.2^\circ N$ ²⁷. While even subtle variations in H_2O and CO_2 content may influence fragmentation efficiency, current sampling coverage and particularly volatile data are limited. Therefore our observations indicate that the observed transition in eruptive style is primarily a function of eruption depth. North of $\sim 63.2^\circ N$, volcanoes erupted in water depths shallower than 300 m, where hydrostatic pressure is low enough to allow vesiculation within rising magma⁷¹. We therefore argue that a first-order control for the generation of volcanoclastic products at the flanks of these edifices is through a combination of quench fragmentation and phreatomagmatic eruptions. As exemplified by the 1963–1967 Surtsey eruption, the rapid cooling and thermal contraction of magma upon contact with seawater promoted autoclastic fragmentation and the formation of initial hyaloclastite breccias⁶. As eruption intensity increased, external water explosively interacted with ascending magma, driving phreatomagmatic activity and producing abundant volcanoclastic deposits⁷¹.

The internal structure of Surtsey is well documented from drilling and geophysical studies^{7,8}. The edifice grew from an initial fissure eruption and consists of overlapping tephra cones composed primarily of unconsolidated to variably palagonitized tephra (60–70% tephra) emplaced by successive phreatomagmatic explosions⁷. These deposits dip 20 – 35° outward from the eruption center, characteristic of tuff cones and rings^{7,8}. Hydrothermal alteration has transformed the inner tephra sequence into palagonite tuff, forming a dense and erosion-resistant core, while effusive phases produced pahoehoe and minor ‘a’ flows that spread southward, locally overlying the tephra cones^{7,8}.

By analogy, we interpret the incoherent seismic signatures at the centers of the Reykjanes edifices (Figs. 3, 4) as zones of brecciated hyaloclastites from initial eruption phases⁴⁸, or hydrothermally altered palagonite tuff. Today, hydrothermal activity on the northern Reykjanes Ridge appears spatially limited, with fluid flow largely restricted to a few fault-controlled sites¹⁵, but it may have been transient and more active shortly after eruption, waning as the volcanic edifice cooled and fluid pathways became sealed. Vertically aligned, high-amplitude reflections (e.g., Fig. 4b) likely represent more solid conduit zones consisting of dykes, which cause acoustic blanking and velocity pull-ups below volcano centers as a result of under-migration of reflections overlain by laterally confined high-velocity anomalies⁴⁸ (Figs. 3d, 4a, b, d). We relate the stratified flanks of the Reykjanes Ridge edifices to products of phreatomagmatic explosions typical of Surtseyan-style eruptions.

These eruptions generate eruption-fed density currents that transport and deposit fragmented tephra, lapilli, spatter, and lithic blocks downslope, forming well-bedded tuff cones and aprons^{72,73}. Experimental and field studies have demonstrated that eruption-fed density currents are capable of efficient particle sorting and lateral dispersal of volcanoclastic material, resulting in broad, low-profile volcanic morphologies^{73,74}. Compared to subaerial plumes, eruption columns in water lose momentum faster due to higher density and viscosity of the surrounding fluid^{175,76}. However, the reduced density contrast between particles and water facilitates suspension of equivalently sized clasts at lower upward velocities than in air, promoting effective sorting within eruption-fed density currents⁷⁷. The high porosity and poor consolidation of rapidly quenched clasts^{68,78} further explain the low seismic amplitudes observed within the flanks. The observed stratification in the seismic images can be explained by repeated pulsatory explosions, each depositing fining-upward successions that would create the impedance contrasts imaged in seismic data (Figs. 3, 4). Internal reflections dipping 17 – 29° match the outward-dipping strata at Surtsey⁶ (20 – 35°) and fall within the range documented for tuff cones⁷⁹, which can exhibit bedding angles up to 30° .

Following this interpretation, we conclude that the smooth-shaped volcanoes of the northern Reykjanes Ridge are produced primarily by Surtseyan eruptions. Based on seismic profiles, we estimate approximate

bulk volumes for the imaged edifices to range from 0.12 km^3 (Fig. 4a) to 0.48 km^3 (Fig. 3c) (Supplementary Table S2). These values are calculated only for the upper portions of the edifices where a clear basal reflection can be identified; the total volumes are therefore likely larger. Even so, they fall below the total bulk volume of the 1963–1967 Surtsey eruption⁶ (1.1 – 1.2 km^3) or that of Black Point Volcano⁷² ($\sim 0.8 \text{ km}^3$) but exceed the estimated volumes of the satellite vents Syrtlingur and Jólnir ($\sim 0.07 \text{ km}^3$ each) and Surtla⁶ ($\sim 0.01 \text{ km}^3$). Future surveys with more closely spaced seismic profiles will be required to refine these estimates and constrain the total erupted volumes of the northern Reykjanes Ridge volcanoes.

The volcanoes south of $\sim 63.2^\circ N$ on the Reykjanes Ridge show no seismically resolvable indicators of volcanoclastic material and appear to be dominated by effusive eruptions (Figs. 1b, d and 3b), which we attribute primarily to greater eruption depths. In mafic systems, the water depth, and thus hydrostatic pressure, exerts a critical control on eruptive style⁷¹. While explosive activity is generally limited to eruptions shallower than ~ 500 m, most documented phreatomagmatic eruptions originate from depths of $<200 \text{ m}$ ⁷¹.

At the Reykjanes Ridge, the transition from dominantly effusive to explosive volcanism occurs at water depths lower than 300 m. At greater water depths, we observe no geophysical evidence of substantial volcanoclastic deposition, suggesting that the greater hydrostatic pressure may suppress explosive magma–water interaction. We note that fragmentation of mid-ocean ridge basalts has been documented at much greater depths in the form of volatile-driven Strombolian activity⁸; however, these eruptions differ fundamentally from the shallow-water processes discussed here, as they are not driven by external water interaction and typically involve lower volatile contents and limited dispersal¹⁴. The observed transition depth of ~ 300 m may have been lower at the time of eruption because relative sea level at the northern Reykjanes Ridge was shaped by the complex interplay of global eustatic change (low stand of ~ 120 m at the LGM; rapid rise to near-present by $\sim 7 \text{ ka}$)⁸⁰ and regional glacio-isostatic rebound⁸¹, implying that the observed transition depth of 300 m from present-day bathymetry may not reflect the true depth limit for phreatomagmatic activity.

Origin of flat-topped morphologies

Characteristic morphological features of the volcanoes north of $\sim 63.2^\circ N$ include smooth topography, flat summits, and exceptionally low H/W ratios compared to other seamounts (Fig. 2 and Supplementary Fig. S1, S2). We discuss three hypotheses to explain this distinctive morphology: (i) formation through effusive eruptions producing flat-topped and shield volcanoes^{28,29}; (ii) construction under ice confinement⁸²; (iii) influence of the sea surface on eruption dynamics and post-eruptive erosion.

Hypothesis (i) Volcanoes located north of $\sim 63.2^\circ N$ show morphological similarities to flat-topped volcanoes and shield volcanoes^{28,29} (Fig. 2l), which typically result from low-viscosity, effusive eruptions. Their formation is governed by a combination of eruptive parameters, including magma viscosity, effusion rate, eruption duration, feeder dike geometry, and the morphology of the underlying seafloor^{28,83}. However, reflection seismic profiles suggest a dominant Surtseyan, rather than purely effusive, activity. We therefore reject this hypothesis.

Hypothesis (ii): Flat summits and low H/W ratios are characteristic of volcanic edifices formed under ice confinement and record direct interaction between magma and ice or meltwater^{78,79}. On land, such morphologies, including tuyas and elongate hyaloclastite ridges, are well-documented onshore Reykjanes Peninsula⁸⁴ and are attributed to subglacial eruptions. Such eruptions can generate intense fragmentation beneath thick ice, as observed during the Gjalp eruption of 1996 beneath 750 m of ice⁸⁵. A notable spatial correlation exists between the southern limit of the Last Glacial Maximum ice cover and the transition from hummocky volcanic edifices to smoother, low H/W morphologies at $\sim 63.2^\circ N$ (Fig. 5a, b), suggesting potential ice-constrained formation. However, several observations contradict this hypothesis:

- (a) Seismic profiles show that the volcanic aprons overlie the erosion unconformity that we relate to the Last Glacial Maximum, implying

- eruption ages younger than 20 ka (Figs. 3, 5), by which time ice cover had largely retreated.
- While internal faulting is evident (Fig. 3c, d), both seismic data and bathymetry show no surface faulting on these volcanoes (Figs. 1f, g, 3c, d, 4, 5c, d). Given the Reykjanes Ridge spreading rate (18–20 mm/yr)^{86,87}, approximately 360–400 m of extension would have occurred since the last glacial maximum. If the edifices had formed during this time, surface faulting would likely be visible¹⁴;
 - Even recently formed volcanic edifices, such as the volcano formed during the 1783 eruption of Nýey¹⁵, exhibit flat summits and low H/W ratios (Figs. 2g, 3d, 5c), clearly demonstrating that ice confinement is not required to produce the observed morphologies. Further, dredged samples from the northern Reykjanes Ridge have been reported to consist of fresh basaltic rock with no evidence of glacial debris or clays and suggested to imply in situ postglacial formation²¹ (Supplementary Fig. S1).

We therefore exclude subglacial volcanism as the origin of the observed morphology and suggest that most volcanoes north of ~63.2°N formed after the Last Glacial Maximum (Fig. 5).

Hypothesis (iii): Eruption depth and sea-level variations are key factors controlling the dynamics of submarine volcanic eruptions and the resulting morphology of volcanoes formed in shallow water depths^{39,75}. Flat-topped morphologies can result from interaction between eruption columns and the sea surface, combined with post-eruptive erosion down to the storm wave base⁸⁸. The abrupt density contrast between water and air can cause submarine eruption columns to spread laterally upon reaching the surface, forming thin eruption umbrellas^{75,89}. Particles within this umbrella may be displaced by ocean currents⁷⁵ and further redistributed by tides and bottom currents. Explosive submarine volcanoes with H/W ratios below ~0.12 have been proposed to be indicative of lateral eruption-column spreading in shallow water⁸⁹ (Fig. 2l).

The studied edifices along the Northern Reykjanes Ridge have even lower H/W ratios (average ~0.07) that are more similar to those of submarine Surtseyan edifices Syrtlingur (H/W ~ 0.09), Jólnir (H/W ~ 0.07), and Surtla (H/W ~ 0.12) near Surtsey⁸ (Fig. 2l), indicating that additional processes may have influenced their morphology. An onshore analogue is Black Point volcano (California), a subaqueous to emergent Surtseyan cone ~120 m high and ~1.6 km wide⁷² (H/W ~ 0.08). Deposits at Black Point show that non-buoyant pyroclasts were redistributed laterally by density currents in addition to fallout⁷². We therefore infer that the low H/W ratios of the Reykjanes Ridge edifices reflect a combination of limited column rise at shallow water depths and lateral dispersal by eruption-fed density currents, together producing their broad, flat-topped morphologies.

An exception is the small volcanic cone imaged in Figs. 3b and 4d. Located at a greater water depth (~300 m), this cone exhibits slightly steeper flanks (~29°) compared to the other volcanoes (17–23°) and lacks a flat summit, resembling deeper-water volcanic cones^{58,59}. At these depths, the higher hydrostatic pressure likely limited plume rise and prevented sustained eruption-column spreading⁸⁹. Instead, eruptions would have been dominated by magma–water interaction near the vent, generating eruption-fed density currents that collapsed rapidly and deposited material downslope^{72,74}. These processes may account for the steeper cone morphology, in contrast to the shallow-water edifices where plume spreading and eruption-fed density currents interacted to build broad, flat-topped volcanoes.

In addition to eruption dynamics, post-eruptive erosion likely further shaped the flat-topped morphology of the edifices north of ~63.2°N. The toplap terminations observed at the summits of the edifices north of ~63.2°N are an indication of erosional truncation. In the Vestmannaeyjar area south of Iceland, storm wave base activity has been observed down to ~45 m depth⁹⁰. Surtla volcano further illustrates wave erosion, as during its eruption in late December 1963 it was inferred to have lied close to sea-level, but within just 17.5 years, the edifice was eroded down to 45 m below sea level, forming a flat-topped plateau at the storm wave base⁹⁰. In our study area, we

observe flat-topped volcanoes with toplap terminations at water depths of up to ~95 m, suggesting that some of these edifices may have formed and subsequently eroded during times of sea level.

Based on the combined evidence from morphology, seismic imagery, and historical analogues, we accept Hypothesis (iii) as the most plausible explanation for the smooth topography, flat summits and low H/W ratios of the volcanoes North of ~63.2°N.

Subaerial volcanism on the Northern Reykjanes Ridge

If a volcanic edifice reaches very shallow water depths, the momentum in the column can allow it to breach the sea surface, as occurred during the formation of Surtsey⁶. Volcanoes on the northern Reykjanes Ridge may reach such shallow depths either because eruptions nucleate on pre-existing topographic highs or older edifices, or because a new cone grows from deeper water during a single eruptive episode, analogous to Surtsey⁶. Our data do not allow us to distinguish unequivocally between these scenarios at individual cones, and we therefore treat them as plausible alternatives.

Historical records show that several of the studied volcanoes breached the sea surface forming islands that were subsequently eroded^{14,15}, and deposited tephra onshore Reykjanes Peninsula^{91,92} (Fig. 1b). Figures 3d and 5c show a seismic profile crossing a volcano associated with a historical eruption that formed the island of Nýey¹⁵, showing internal unconformities and a horizontal, terrace-like reflection. This feature could either reflect episodic eruptive construction or erosional modification during or after emplacement. We estimate an approximate bulk volume of 0.41 km³ for the uppermost part of the edifice (Fig. 3d).

Nýey was first discovered on 1 May 1783 by Jörgen Mindelberg, the captain of the Danish fishing vessel Boesand, who observed smoke rising from the sea southwest of the Reykjanes Peninsula (Kleemann⁹³ and citations therein). However, given the severe smoke and sulfuric smell, he found it impossible to inspect the island. As the smoke intensified, it became noticeable to the inhabitants of mainland Iceland. Danish fishermen aboard the *Torksen* reported a burning island that was surrounded by pumice, smoke, and fire, obstructing sea travel in the area. During the summer of 1783, Nýey received attention in the European press⁹³, but following inspection expeditions found that Nýey had vanished by spring 1784.

Today, the remains of the island lie at a depth of approximately 40 m. Images acquired by the OFOS show that the top of this volcano is characterized by rounded boulders and rounded rock fragments atop of cobbles (Fig. 3e and Supplementary Fig. S4). The central part of the now-submerged Nýey volcano is characterized in the bathymetry by a hummocky surface (Fig. 1f) and in seismic data by acoustic blanking at the center without stratification (Figs. 3d and 5c), indicating the presence of attenuating volcanic lithologies. The rounded boulders are thus likely the products of erosion of lava flows and/or the vent region of the edifice. Although historical reports support the generation of volcanoclastic material during the eruption of Nýey⁹³, the absence of finer materials in the seafloor imagery suggests prolonged exposure to high-energy conditions and substantial post-eruptive erosion (Fig. 3e).

These observations resemble those at Surtla volcano⁹⁰, whose summit plateau consists of predominantly basalt blocks with only a minor component of fine sediments, interpreted as evidence that the present-day surface does not represent the primary volcanic deposit⁹⁰. In both cases, Surtla and Nýey, the larger blocks appear to have remained roughly in place, gradually subsiding as underlying support was removed⁹⁰. A similar fate befell Syrtlingur, a tephra island that briefly rose ~70 m above sea level in 1965 but was destroyed by waves within weeks of eruptive cessation; today, its summit lies at ~43 m depth⁹. Jólnir, formed southwest of Surtsey between 1965 and 1966, likewise reached ~70 m elevation before being completely eroded by late 1966; it now represents a flat-topped submarine plateau at ~34 m depth⁹.

Other volcanoes of the Northern Reykjanes Ridge may also have breached the surface, given the inferred occurrence of lava flows on top of stratified deposits at several volcanoes, most prominently visible by the

edifice imaged in Fig. 4e. Surtseyan eruptions commonly begin with phreatomagmatic explosions, but once the vent breaches the water–air interface and becomes isolated from direct water interaction, activity may transition to magmatic, typically effusive or Strombolian⁶. The subaerial eruptive activity produces lava that, when solidified, is more resistant to coastal erosion than loose tephra⁶.

Conclusions

The Reykjanes Ridge is one of the few places on Earth where a mid-ocean ridge approaches land, providing a unique setting to investigate submarine volcanism across a depth gradient. By combining high-resolution bathymetry and seismic reflection data, we identify characteristic patterns of both effusive and explosive volcanism and relate them to eruption dynamics and post-eruptive modification. We define a spatial window between ~63.2°N and the Icelandic coastline where shallow marine conditions favoured recurrent Surtseyan eruptions.

Our study shows:

- (i) Effusive eruptions dominate in deeper water (> 300 m) south of ~63.2°N, forming rugged edifices with no internal stratification and pronounced seismic attenuation (Fig. 6a).
- (ii) Phreatomagmatic eruptions occur in shallower water (< 300 m) north of ~63.2°N, producing smoother volcanoes with stratified flanks, comprising volcanoclastic deposits (Fig. 6b, c).
- (iii) Most phreatomagmatic eruptions post-date the Last Glacial Maximum (~20 ka).
- (iv) Low height/width ratios of the volcanoes result from eruption column spreading at the water–air interface in shallower water depths and lateral dispersal by eruption-fed density currents, forming prograding and toplapping volcanoclastic deposits with low H/W ratios (~0.07) (Fig. 6d, e).
- (v) Some volcanoes breached the sea surface, transitioning into subaerial activity and depositing Strombolian and effusive materials atop older phreatomagmatic units (Fig. 6h).
- (vi) Post-eruptive erosion down to the storm wave base further sculpted flat-topped summits, as demonstrated by the rapid erosion of short-lived volcanic islands such as Nýey (Fig. 6i).

Historical records show that several eruptions along Northern Reykjanes Ridge have breached the sea surface in the last 1000 years. During this time, none of the eruptions have noticeably impacted the coastal communities of Iceland⁹⁴, although smoke from the eruption of Nýey in 1783 was noted onshore Reykjanes Peninsula⁹³ and an offshore phreatomagmatic eruption in 1226 CE deposited tephra on Reykjanes Peninsula^{91,92}. Our study shows that such eruptions have been common on the Northern Reykjanes Ridge since the Last Glacial Maximum. Future eruptions along the Northern Reykjanes Ridge may have localized impacts on submarine infrastructure, such as subsea telecommunication cables⁹⁵, as well as nearby boats.

Submarine volcanoes remain difficult to study because of their inaccessibility, structural complexity, and post-eruption modification. While direct sampling is invaluable for further ground truthing and for determining the driving force of explosivity by constraining lithology, volatile content, and detailed eruptive processes, it is often spatially limited due to poor exposure, burial of primary deposits, and the technical challenges of recovering unconsolidated clastic material. Our study helps overcome these limitations by providing first-order seismic and morphological identification criteria submarine volcanic processes. These criteria can be applied to other submarine volcanic provinces to help refine global eruption records and close the current blind spot in volcanology regarding submarine explosive volcanism. To advance beyond first-order estimates on the Northern Reykjanes Ridge, future campaigns should combine high-resolution seismic surveys with dedicated sampling. Denser seismic profiling will enable more accurate volumetric reconstructions, while targeted sampling will allow ground-truthing of lithological interpretations and eruption dynamics. Only such integrated approaches can fully resolve the role of explosive volcanism in shaping submarine volcanic systems.

Methods

Bathymetry and topography data

High-resolution bathymetry of the northern Reykjanes Ridge until between ~62.7°N and ~63.3°N was obtained from the Marine and Freshwater Research Institute (MFRI) in Iceland. The raw multibeam data were processed and gridded using *CARIS HIPS & SIPS* software (20 × 20 m cell size) in the ISN2004 projection. This dataset was complemented by global bathymetry from the GEBCO 2023 Grid. Additionally, topographic data from the Reykjanes Ridge region (10 × 10 m cell size) were sourced from the ArcticDEM project⁹⁶. All datasets were imported into a unified QGIS project (version 3.34.15-Prizren). Bathymetric profiles presented in Fig. 2a–k were extracted using the QGIS Profiler Plug-In. Dimensions of the submarine volcanoes Jólnir, Syrtlingur, and Surtla were estimated by georeferencing published bathymetric maps⁹.

Roughness estimation

We extracted 44 topographical profiles from the high-resolution bathymetry and onshore elevation datasets to analyse and quantify the large-scale relative surface roughness (Fig. 2l). Each profile consisted of elevation measurements sampled at variable spatial intervals along linear transects oriented perpendicular to morphological features. To ensure comparability across profiles and reduce bias from resolution differences, all elevation data were interpolated onto a uniform spatial grid with 20 m spacing. This resampling step normalized the effective resolution of each profile. Note that this measure is therefore not sensitive to roughness below 20 m.

Local slope was then computed as the first-order finite difference of elevation with respect to distance, i.e., the discrete derivative of the interpolated topography. We define surface roughness as the standard deviation of the slope values along each profile. This metric captures short-wavelength variability in surface gradients and provides a scale-independent measure of morphological complexity, consistent with prior work in geomorphometry^{23,24}.

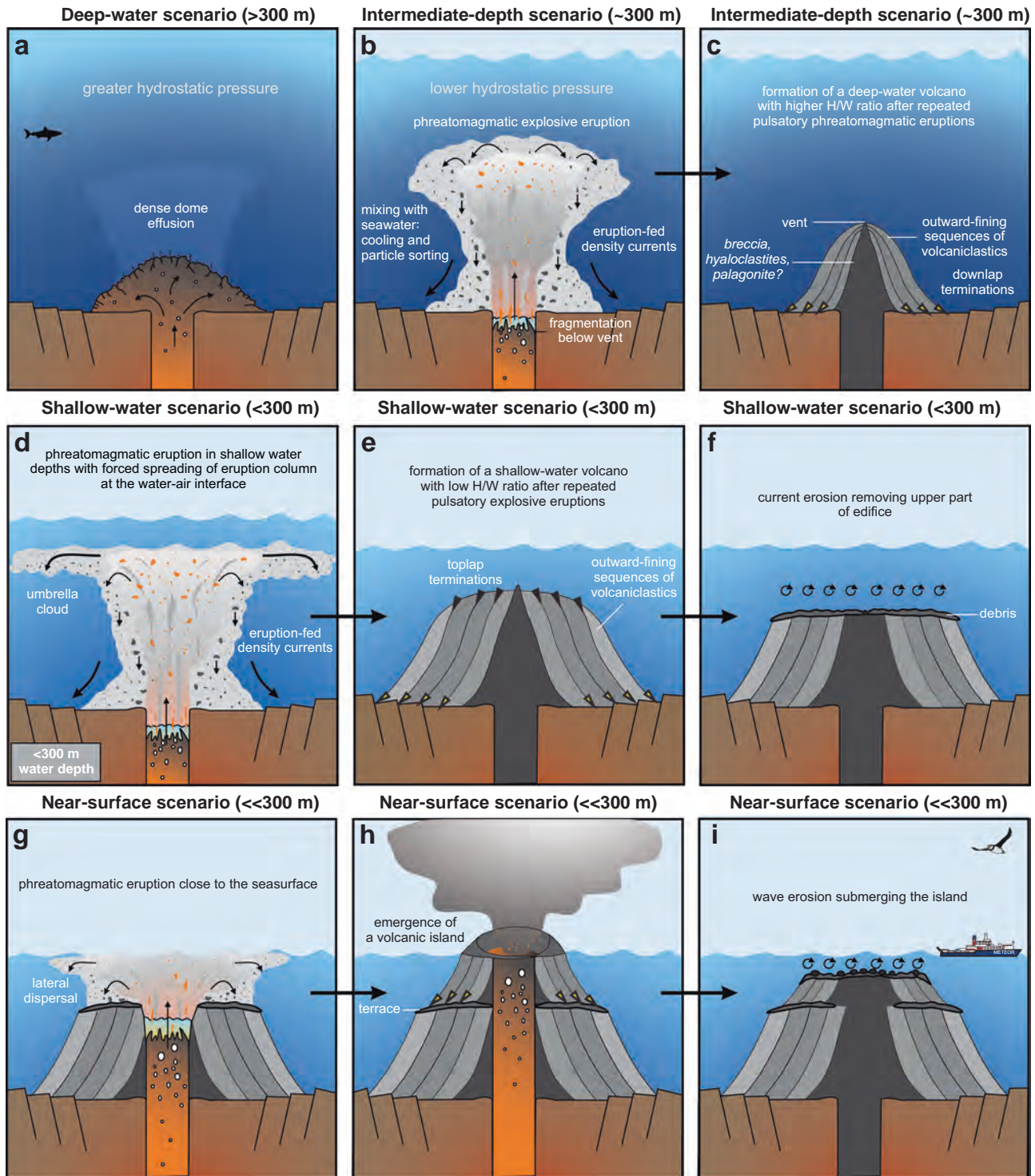
To integrate and compare roughness across profiles with varying lengths, resolutions, and terrain types, we applied a normalization and weighting procedure. First, roughness values were normalized by the number of slope measurements, accounting for differences in profile lengths and the number of contributing segments. We then used a weighted combination scheme, in which confidence intervals—derived from the standard error of the slope distribution and the Student's *t* distribution—were used to estimate the statistical reliability of each roughness value. These weights effectively down-weight profiles with large uncertainty due to short length or high variability, enabling a more balanced representation of roughness across the dataset.

All processing and analysis were performed in MATLAB R2024a. The full code is provided in the Supplementary Information. Profile locations of all measurements are shown in Supplementary Fig. S3, and roughness estimates with associated uncertainties are summarized in Supplementary Table S1.

Seismic data acquisition and processing

During Expedition M201 we conducted seismic surveys following Joint Nature Conservation Committee mitigation standards to minimize environmental impact²². The seismic source was an array of two GI-Guns towed at approximately 2 m depth. For the Reykjanes Ridge profiles presented in this study we used a single G. I. Gun in True GI Mode (Generator Vol.: 45 in³, Injector Volume: 105 in³) with a shot interval of 4 seconds. Seismic data were recorded with a 120-channel Hydrosience Technologies SeaMUX digital streamer (500 m active length) equipped with Concord Navigator birds and towed at 4 m depth. Recording lengths ranged from 1 to 6 s depending on water depth, and data were recorded at 1 ms and stored in SEG-Y format.

Onboard pre-processing was performed using Schlumberger Vista, and included assigning source and receiver coordinates, crooked-line common-midpoint (CMP) binning at 10 m intervals, lowpass filtering (at 10 Hz) to attenuate swell noise and de-spike to remove electrical



interference. A sparse velocity field was also picked using semblance analysis on unmigrated CMP gathers.

We performed further onshore seismic data processing using Shearwater Reveal. The onshore flow included trace edit (removal and interpolation of persistently noisy channels), and shot scaling based on the amplitude of the direct arrival to boost several series of persistently weak shots. This was followed by a variable-depth de-ghost (receiver-side only), de-bubble and zero-phase conversion. The source signature for de-bubble and zero-phase conversion was estimated by shift-stacking the near-trace seafloor reflection for incidence angles $>20^\circ$ for all profiles⁹⁷. A single de-bubble operator for all traces was derived using a predictive deconvolution

(24 ms gap, 2% pre-whitening) to attenuate the bubble pulse. The zero-phase conversion operator was generated using a match filter between the de-bubbled source signature and its zero-phase equivalent, and similarly applied to all traces, rotating the phase of the wavelet from approximately minimum-phase to approximately zero-phase. As only a very small amount of the reflected energy was above 200 Hz, we resampled the data to 2 ms (including an anti-aliasing filter) to reduce the data size and improve computation time for further processing steps. We then performed surface-related multiple elimination (SRME) to attenuate multiples associated with the sea surface and applied a pre-stack phase-Q compensation ($Q = 120$ below the seafloor) to correct for dispersion effects. We then performed a

Fig. 6 | Conceptual model of the formation of effusive and explosive volcanoes at the Reykjanes Ridge. **a** Formation of effusive volcanoes in water depths greater than ~300 m. Size of vent is strongly exaggerated. **b, c** Formation of a phreatomagmatic volcano in greater water depths (~300 m). At these depths, limited plume rise prevents sustained eruption-column spreading (b). Instead, magma–water interaction near the vent produces eruption-fed density currents that disperse volcanoclastic material, producing an outward-fining sequence with smooth topography (c). Characteristic features are well-stratified flanks and low H/W ratios⁷² (>0.12). **d–f** Formation of phreatomagmatic volcano in shallow water depths (<300 m). Here, eruptions involve both eruption-fed density currents and eruption-column spreading at the sea surface. The plume reaches the water–air interface (d), where the density contrast forces lateral spreading into an umbrella cloud while density currents continue to transport non-buoyant pyroclasts downslope. Together, these processes produce low (<0.12) H/W ratios, stratified flanks, and internal toplap

terminations (black arrows) (e). Subsequent erosion down to the storm-wave base can truncate the summit and form terrace-like surfaces (f). (g–i) Formation of a volcano in shallow-water settings. Phreatomagmatic explosions in very shallow water can generate eruption columns that occasionally breach the sea surface (g). Volcanoes may reach such shallow depths either because eruptions initiate on pre-existing topographic highs or older edifices, or because a new cone grows upward during a single eruptive episode. Once a volcano has reached very shallow water depths, the momentum of the eruption may breach the sea surface forming a volcanic island (h). As the vent becomes subaerial, the eruption becomes eventually dry and transitions towards Strombolian eruptions and effusive lava flows (h). With time, current erosion submerges the volcano (i). The surface may be characterized by rounded boulders as observed in OFOS imagery on top of the edifice that formed the island of Nýey (Fig. 3d). Panels are not to scale and vertically exaggerated.

semblance-based migration velocity analysis (2 km interval) on pre-stack time migrated (PSTM) CMP gathers migrated with the sparse velocity field picked offshore.

The final migration included offset regularisation using a partial moveout correction and a Kirchhoff PSTM (including a geometric spreading correction) using the picked migration velocity field. This was followed by semblance-based stacking velocity analysis (1 km interval) to further flatten the reflectors before stacking. Post-migration we performed a parabolic Radon de-multiple and de-noise with a seafloor-relative Radon mute and an automated residual moveout (RMO) correction (50 m interval). We then applied a 30° outer angle mute (preserving 200 m near-offset) to remove post-critical refractions, NMO stretch, and mode-converted energy and stacked the data to obtain the migrated image.

Post-stack we applied an amplitude-Q compensation ($Q = 120$ below the seafloor) to correct for attenuation and improve the resolution of deeper reflectors. This was followed by time-variant bandpass filtering (relative to the seafloor) to attenuate both low- and high-frequency noise, an amplitude boost of +10 dB/s below the seafloor to further balance the amplitudes for interpretation, and a top mute above the seafloor reflection.

Volume and dip estimation

We estimated the volumes of several flat-topped volcanic edifices using a semi-quantitative approach constrained by limited profile coverage—each volcano was typically crossed by only a single seismic line (Supplementary Fig. S6 and S7). First, we picked the base of each edifice in Kingdom software and interpolated this surface at a resolution of 20×20 m. This interpolation is only applicable to volcanoes with a well-defined base and assumes a laterally flat basal horizon, an approximation partly justified by the observation that most edifices evolved atop terrace-like morphologies. Next, we delineated the approximate lateral extent of each edifice based on bathymetric data. This step introduces additional uncertainty, as the true boundaries of the edifices are not always clearly defined. Note that we have chosen a conservative approach for delineating the extent of the volcanic edifices and, thus, the derived volumes are likely minimum estimates.

To estimate thicknesses, we converted seafloor depth from bathymetry to two-way travel time (TWT) using a water velocity of 1500 m/s, then subtracted this surface from the interpolated basal horizon within Kingdom. The resulting TWT difference maps were exported as and further processed in MATLAB, where we calculated edifice volumes (Supplementary Table S2 and Supplementary Fig. S6). For this step, we assumed a P-wave velocity of 1560 m/s, consistent with measurements on basaltic volcanoclastic sediments recovered by IODP Expedition 396 from the Norwegian Margin⁹⁸ with minimum and maximum values ranging between 1500–1650 m/s (see Supporting Information for Matlab script).

In addition, we estimated bedding dips from time-migrated seismic profiles (Figs. 3, 4). Dip directions were picked manually, and angles were calculated using the same P-wave velocity (1560 m/s). Because these estimates are based on time-migrated rather than depth-migrated data, they carry an inherent uncertainty. We therefore interpret the reported dip

angles as first-order approximations, suitable for comparing relative differences between edifices rather than for providing precise structural measurements.

Ocean Floor Observatory System (OFOS)

Ocean Floor Observation System (OFOS) is a lowerable, passively towed frame equipped with cameras and light meant to image the ocean floor for visual reference. Two metal fins at the back of the OFOS steel frame increased drag and effectively stabilized the system while being towed. The OFOS system is equipped with both a photo camera (Ocean imaging system (OIS), Nikon D7100, 24.1 Mpx) and a high-definition video camera (Canon HF-G10,1080p at 25 fps, 10× optical zoom). The OIS photo camera works autonomously and has been programmed to start image acquisition after a set delay at a 2-s interval. The camera has been set to automatic mode without flash usage. Furthermore, a GoPro HERO 12 black recording at 5.3 K resolution (5312 × 4648 pixel, 24 fps, 10Bit, 24.7 Mpx) in a high-pressure camera housing has been mounted to the OFOS next to the HD camera. The images are stored in the onboard memory of the individual cameras and will be extracted after the dive. The cameras are mounted, looking down with a slight tilt towards the center. Two laser pointers surrounding the video camera at an equidistance of 50 cm were used to estimate the size of seafloor objects. The lighting system consists of three dimmable high-power LED lights and a pressure-neutral 4x LED array developed by GEOMAR (2x Sealite Sphere 5150, 1x Teledyne Bowtech). The OFOS has an additional battery-powered 5000 K LED light featuring 3500 lumens. The OFOS is equipped with a USBL positioning system (iXBlue Posidonia) to track the position of the system at decimeter accuracy. The OFOS is lowered from the ship's side crane with the 18 mm Coaxial Cable to allow for live video preview. The winch operator sits in the OFOS control room and manually adjusts the height above the seafloor. The ship tows the OFOS with up to 0.5 kn along a pre-determined profile facing against the present current. Pictures have been taken with high overlap. The photos of small transects have been assembled using photogrammetry (Apple Object Capture API) into 3D models of the ocean floor. Such 3D models have been rendered using Blender (Supplementary Fig. S4).

Data availability

All seismic data shown in this study are accessible at Zenodo data repository (<https://doi.org/10.5281/zenodo.14500271>).

Code availability

The MATLAB scripts used for calculating relative roughness values and estimating approximate volcanic edifice volumes are available in the Supplementary Information.

Received: 14 March 2025; Accepted: 11 December 2025;
Published online: 31 December 2025

References

1. Watts, A. B., Sandwell, D. T., Smith, W. H. & Wessel, P. Global gravity, bathymetry, and the distribution of submarine volcanism through space and time. *J. Geophys. Res. Solid Earth* **111**, B08408 (2006).
2. Helo, C., Longpré, M. A., Shimizu, N., Clague, D. A. & Stix, J. Explosive eruptions at mid-ocean ridges driven by CO₂-rich magmas. *Nat. Geosci.* **4**, 260–263 (2011).
3. Sohn, R. A. et al. Explosive volcanism on the ultraslow-spreading Gakkel ridge, Arctic Ocean. *Nature* **453**, 1236–1238 (2008).
4. Clague, D. A., Paduan, J. B. & Davis, A. S. Widespread strombolian eruptions of mid-ocean ridge basalt. *J. Volcanol. Geotherm. Res.* **180**, 171–188 (2009).
5. Preine, J. et al. Tracing the Neovolcanic zone along the sediment-covered regions of the Red Sea Rift. *Sci. Rep.* **15**, 5481 (2025).
6. Thorarinsson, S. The Surtsey eruption: course of events during the year 1967. *Surtsey Res. Prog. Rep.* **4**, 143–148 (1968).
7. Jakobsson, S. P. & Moore, J. G. The Surtsey research drilling project of 1979. *Surtsey Res. Prog. Rep.* **9**, 76–93 (1982).
8. Schipper, C. I., Jakobsson, S. P., White, J. D., Palin, J. M. & Bush-Marcinowski, T. The Surtsey magma series. *Sci. Rep.* **5**, 11498 (2015).
9. Jakobsson, S. P., Thors, K., Vésteinsson, Á. T. & Ásbjörnsdóttir, L. Some aspects of the seafloor morphology at Surtsey volcano: the new multibeam bathymetric survey of 2007. *Surtsey Res.* **12**, 9–20 (2009).
10. Nichols, A. R. L., Carroll, M. R. & Höskuldsson, Á. Is the Iceland hot spot also wet? Evidence from the water contents of undegassed submarine and subglacial pillow basalts. *Earth Planet. Sci. Lett.* **202**, 77–87 (2002).
11. Moore, J. G. & Schilling, J. G. Vesicles, water, and sulfur in Reykjanes Ridge basalts. *Contrib. Mineral. Petrol.* **41**, 105–118 (1973).
12. Jambon, A. & Zimmermann, J. L. Major volatiles from a North Atlantic MORB glass and calibration to He: a size fraction analysis. *Chem. Geol.* **62**, 177–189 (1987).
13. Jakobsson, S. P. & Moore, J. G. Hydrothermal minerals and alteration rates at Surtsey volcano, Iceland. *Geol. Soc. Am. Bull.* **97**, 648–659 (1986).
14. Höskuldsson, A., Hey, R., Kjartansson, E. & Gudmundsson, G. The Reykjanes Ridge is between 63°10' N and Iceland. *J. Geodyn.* **43**, 73–86 (2007).
15. Pałgan, D., Devey, C. W. & Yeo, I. A. Volcanism and hydrothermalism on a hotspot-influenced ridge: comparing Reykjanes Peninsula and Reykjanes Ridge, Iceland. *J. Volcanol. Geotherm. Res.* **348**, 62–81 (2017).
16. Egloff, J. & Johnson, G. L. Erosional and depositional structures of the southwest Iceland insular margin: thirteen geophysical profiles. *Marine Geology: Am. Assoc. Petrol. Geol., Tulsa, Oklahoma.* **109**, 43–63 (1979).
17. Hubbard, A., Sugden, D., Dugmore, A., Norddahl, H. & Pétursson, H. G. A modelling insight into the Icelandic Last Glacial Maximum ice sheet. *Quat. Sci. Rev.* **25**, 2283–2296 (2006).
18. Norðdahl, H., Ingólfsson, Ó., Pétursson, H. G. & Hallsdóttir, M. Late Weichselian and Holocene environmental history of Iceland. *J.ökull.* **58**, 343–364 (2008).
19. O'NIONS, R. K., Pankhurst, R. J. & Gronvold, K. Nature and development of basalt magma sources beneath Iceland and the Reykjanes Ridge. *J. Petrol.* **17**, 315–338 (1976).
20. Brooks, C. K., Jakobsson, S. P. & Campsie, J. Dredged basaltic rocks from the seaward extensions of the Reykjanes and Snaefellsnes volcanic zones, Iceland. *Earth Planet. Sci. Lett.* **22**, 320–327 (1974).
21. Johnson, G. L. & Jakobsson, S. P. Structure and petrology of the Reykjanes Ridge between 62° 55' N and 63° 48'. *N. J. Geophys. Res. Solid Earth*, **90**, 10073–10083 (1985).
22. Augustin, N. et al. *Volcanism in the Vesturdjúp Basin-Flank Igneous System or Intraplate Volcanism Off-Shore Western Iceland* (Institut für Geologie, Universität Hamburg, Leitstelle Deutsche Forschungsschiffe, 2024).
23. Evans, I. S. General geomorphometry, derivatives of altitude, and descriptive statistics. in *Spatial Analysis in Geomorphology*, 17–90 (Routledge, 2019).
24. Grohmann, C. H., Smith, M. J. & Riccomini, C. Multiscale analysis of topographic surface roughness in the Midland Valley, Scotland. *IEEE Trans. Geosci. Remote Sens.* **49**, 1200–1213 (2010).
25. Kennish, M. J. & Lutz, R. A. Morphology and distribution of lava flows on mid-ocean ridges: a review. *Earth-Sci. Rev.* **43**, 63–90 (1998).
26. Jakobsson, S. P., Jónsson, J. & Shido, F. Petrology of the western Reykjanes peninsula, Iceland. *J. Petrol.* **19**, 669–705 (1978).
27. Le Saout, M. et al. Variations in volcanism and tectonics along the hotspot-influenced Reykjanes Ridge. *Geochem. Geophys. Geosyst.* **24**, e2022GC010788 (2023).
28. Clague, D. A., Moore, J. G. & Reynolds, J. R. Formation of submarine flat-topped volcanic cones in Hawai'i. *Bull. Volcanol.* **62**, 214–233 (2000).
29. Rossi, M. J. & Gudmundsson, A. The morphology and formation of flow-lobe tumuli on Icelandic shield volcanoes. *J. Volcanol. Geotherm. Res.* **72**, 291–308 (1996).
30. White, J. D. Pre-emergent construction of a lacustrine basaltic volcano, Pahvant Butte, Utah (USA). *Bull. Volcanol.* **58**, 249–262 (1996).
31. Parnell-Turner, R. et al. A continuous 55-million-year record of transient mantle plume activity beneath Iceland. *Nat. Geosci.* **7**, 914–919 (2014).
32. Warwel, A. et al. The Paleozoic hydrocarbon system in the Gotland Basin (central Baltic Sea) leaks. *Earth Space Sci.* **10**, e2023EA002883 (2023).
33. Haimerl, B. et al. Land-to-sea mapping of the glacial erosion unconformity reveals evolution of the Jasmund Glacitectonic Complex east of Rügen Island (SW Baltic Sea). *Geophys. Res. Lett.* **51**, e2024GL111603 (2024).
34. Büker, F., Green, A. G. & Horstmeyer, H. 3-D high-resolution reflection seismic imaging of unconsolidated glacial and glaciolacustrine sediments: processing and interpretation. *Geophysics* **65**, 18–34 (2000).
35. Burschil, T. et al. High-resolution reflection seismics reveal the structure and the evolution of the Quaternary glacial Tannwald Basin. *Surf. Geophys.* **16**, 593–610 (2018).
36. Lackschewitz, K. S. & Wallrabe-Adams, H. J. Composition and origin of volcanic ash zones in Late Quaternary sediments from the Reykjanes Ridge: evidence for ash fallout and ice-rafting. *Mar. Geol.* **136**, 209–224 (1997).
37. Maresch, J., White, R. S., Hobbs, R. W. & Smallwood, J. R. Seismic attenuation of Atlantic margin basalts: Observations and modeling. *Geophysics* **71**, B211–B221 (2006).
38. Nelson, C. E., Hobbs, R. W. & Rusch, R. On the use of fractal surfaces to understand seismic wave propagation in layered basalt sequences. *Pure Appl. Geophys.* **172**, 1879–1892 (2015).
39. Cas, R. A. & Simmons, J. M. Why deep-water eruptions are so different from subaerial eruptions. *Front. Earth Sci.* **6**, 198 (2018).
40. Head, J. W. & Wilson, L. Deep submarine pyroclastic eruptions: theory and predicted landforms and deposits. *J. Volcanol. Geotherm. Res.* **121**, 155–193 (2003).
41. Cahalan, R. C. & Dufek, J. Explosive submarine eruptions: The role of condensable gas jets in underwater eruptions. *J. Geophys. Res. Solid Earth* **126**, e2020JB020969 (2021).
42. Shen, Y., Whittaker, C. N., Lane, E. M., White, J. D. & Power, W. Physical experiments of waves generated by submerged steam eruptions with applications to volcanic tsunamis. *Sci. Adv.* **10**, eadk6208 (2024).

43. Seabrook, S. et al. Volcaniclastic density currents explain widespread and diverse seafloor impacts of the 2022 Hunga Volcano eruption. *Nat. Commun.* **14**, 7881 (2023).
44. Metcalfe, A. et al. Submarine ash megabeds fed by far-traveled, shoreline-crossing pyroclastic currents from a large explosive volcanic eruption. *Sci. Adv.* **11**, eads9642 (2025).
45. Druitt, T. et al. Giant offshore pumice deposit records a shallow submarine explosive eruption of ancestral Santorini. *Commun. Earth Environ.* **5**, 24 (2024).
46. White, J. D. & Houghton, B. F. Primary volcaniclastic rocks. *Geology* **34**, 677–680 (2006).
47. Fisher, R. V. & Schmincke, H. U. Pyroclastic rocks and tectonic environment. in *Pyroclastic Rocks* 383–409 (Springer Berlin Heidelberg, 1984).
48. Reynolds, P., Schofield, N., Brown, R. J. & Holford, S. P. The architecture of submarine monogenetic volcanoes—insights from 3D seismic data. *Basin Res.* **30**, 437–451 (2018).
49. Preine, J. et al. Hazardous explosive eruptions of a recharging multi-cyclic island arc caldera. *Nat. Geosci.* **17**, 323–331 (2024).
50. Mitchell, N. C., Masson, D. G., Watts, A. B., Gee, M. J. & Urgeles, R. The morphology of the submarine flanks of volcanic ocean islands: a comparative study of the Canary and Hawaiian hotspot islands. *J. Volcanol. Geotherm. Res.* **115**, 83–107 (2002).
51. Branney, M. J. & Kokelaar, B. P. *Pyroclastic Density Currents and the Sedimentation of Ignimbrites* (Geological Society of London, 2002).
52. Allen, S. R. Reconstruction of a major caldera-forming eruption from pyroclastic deposit characteristics: Kos Plateau Tuff, eastern Aegean Sea. *J. Volcanol. Geotherm. Res.* **105**, 141–162 (2001).
53. Walker, S. L. et al. Eruption-fed particle plumes and volcaniclastic deposits at a submarine volcano: NW Rota-1, Mariana Arc. *J. Geophys. Res. Solid Earth* **113**, B08S11 (2008).
54. Mitchell, N. C. Susceptibility of mid-ocean ridge volcanic islands and seamounts to large-scale landsliding. *J. Geophys. Res. Solid Earth* **108**, 2397 (2003).
55. Lipman, P. W., Normark, W. R., Moore, J. G., Wilson, J. B. & Gutmacher, C. E. The giant submarine alaka debris slide, Mauna Loa, Hawaii. *J. Geophys. Res. Solid Earth* **93**, 4279–4299 (1988).
56. Planke, S., Symonds, P. A., Alvestad, E. & Skogseid, J. Seismic volcanostratigraphy of large-volume basaltic extrusive complexes on rifted margins. *J. Geophys. Res. Solid Earth* **105**, 19335–19351 (2000).
57. Wright, K. A., Davies, R. J., Jerram, D. A., Morris, J. & Fletcher, R. Application of seismic and sequence stratigraphic concepts to a lava-fed delta system in the Faroe-Shetland Basin, UK and Faroes. *Basin Res.* **24**, 91–106 (2012).
58. Weiß, B. J., Hübscher, C., Wolf, D. & Lüdmann, T. Submarine explosive volcanism in the southeastern Terceira Rift/São Miguel region (Azores). *J. Volcanol. Geotherm. Res.* **303**, 79–91 (2015).
59. Hübscher, C., Ruhnu, M. & Nomikou, P. Volcano-tectonic evolution of the polygenetic Kolumbo submarine volcano/Santorini (Aegean Sea). *J. Volcanol. Geotherm. Res.* **291**, 101–111 (2015).
60. Karstens, J. et al. Cascading events during the 1650 tsunamigenic eruption of Kolumbo volcano. *Nat. Commun.* **14**, 6606 (2023a).
61. Druitt, T. H. et al. Expedition 398 summary. *Proc. Int. Ocean Discov. Program 398* (2024).
62. Preine, J. et al. (2025). Data report: core-seismic integration and time-depth relationships at IODP Expedition 398 Hellenic Arc Volcanic Field sites. In Druitt, T.H., Kutterolf, S., Ronge, T.A., and the Expedition 398 Scientists, Hellenic Arc Volcanic Field. *Proc. Int. Ocean Discov. Program 398* (2024).
63. Carey, S. et al. (2011). Exploration of the Kolumbo volcanic rift zone.
64. Bischoff, A., Rossetti, M., Nicol, A. & Kennedy, B. Seismic reflection and petrographic interpretation of a buried monogenetic volcanic field (part 1). *Bull. Volcanol.* **81**, 1–19 (2019).
65. Bischoff, A., Nicol, A., Barrier, A. & Wang, H. Paleogeography and volcanic morphology reconstruction of a buried monogenetic volcanic field (part 2). *Bull. Volcanol.* **81**, 1–23 (2019).
66. Gase, A. C. et al. Subducting volcaniclastic-rich upper crust supplies fluids for shallow megathrust and slow slip. *Sci. Adv.* **9**, eadh0150 (2023).
67. Steinmann, L., Spiess, V. & Sacchi, M. Post-collapse evolution of a coastal caldera system: Insights from a 3D multichannel seismic survey from the Campi Flegrei caldera (Italy). *J. Volcanol. Geotherm. Res.* **349**, 83–98 (2018).
68. Manga, M. et al. Contrasting seismic velocity and compaction of marine calcareous oozes and volcaniclastic deposits on the South Aegean Volcanic Arc. *Geochem. Geophys. Geosyst.* **26**, e2025GC012327 (2025).
69. Watt, S. F. L. et al. Combinations of volcanic-flank and seafloor-sediment failure offshore Montserrat, and their implications for tsunami generation. *Earth Planet. Sci. Lett.* **319**, 228–240 (2012).
70. Watt, S. F., Karstens, J. & Berndt, C. Volcanic-island lateral collapses and their submarine deposits. in *Volcanic Debris Avalanches: From Collapse to Hazard*, 255–279 (Springer International Publishing, 2020).
71. Valentine, G. A., Graettinger, A. H. & Sonder, I. Explosion depths for phreatomagmatic eruptions. *Geophys. Res. Lett.* **41**, 3045–3051 (2014).
72. Murtagh, R. M. & White, J. D. Pyroclast characteristics of a subaqueous to emergent Surtseyan eruption, Black Point volcano, California. *J. Volcanol. Geotherm. Res.* **267**, 75–91 (2013).
73. Brand, B. D. & Clarke, A. B. The architecture, eruptive history, and evolution of the Table Rock Complex, Oregon: From a Surtseyan to an energetic maar eruption. *J. Volcanol. Geotherm. Res.* **180**, 203–224 (2009).
74. Cantelli, A., Johnson, S., White, J. D. L. & Parker, G. Sediment sorting in the deposits of turbidity currents created by experimental modeling of explosive subaqueous eruptions. *J. Geol.* **116**, 76–93 (2008).
75. Cashman, K. V. & Fiske, R. S. Fallout of pyroclastic debris from submarine volcanic eruptions. *Science* **253**, 275–280 (1991).
76. White, J. D., Smellie, J. L. & Clague, D. A. *Explosive Subaqueous Volcanism*, Vol. 140 (American Geophysical Union, 2003).
77. Sparks, R. S. J. et al. Sediment-laden gravity currents with reversing buoyancy. *Earth Planet. Sci. Lett.* **114**, 243–257 (1993).
78. Manga, M. et al. The pumice raft-forming 2012 Havre submarine eruption was effusive. *Earth Planet. Sci. Lett.* **489**, 49–58 (2018).
79. Wohletz, K. H. & Sheridan, M. F. A model of pyroclastic surge. *Geol. Soc. Am. Spec. Pap.* **180**, 177–194 (1979).
80. Lambeck, K., Rouby, H., Purcell, A., Sun, Y. & Sambridge, M. Sea level and global ice volumes from the Last Glacial Maximum to the Holocene. *Proc. Natl. Acad. Sci.* **111**, 15296–15303 (2014).
81. Ingólfsson, Ó., Norddahl, H. & Haflidason, H. Rapid isostatic rebound in southwestern Iceland at the end of the last glaciation. *Boreas* **24**, 245–259 (1995).
82. Russell, J. K., Edwards, B. R., Porritt, L. & Ryane, C. Tuya: a descriptive genetic classification. *Quat. Sci. Rev.* **87**, 70–81 (2014).
83. Bonatti, E. & Harrison, C. G. A. Eruption styles of basalt in oceanic spreading ridges and seamounts: Effect of magma temperature and viscosity. *J. Geophys. Res. Solid Earth* **93**, 2967–2980 (1988).
84. Höskuldsson, A. & Sparks, R. S. J. Thermodynamics and fluid dynamics of effusive subglacial eruptions. *Bull. Volcanol.* **59**, 219–230 (1997).
85. Gudmundsson, M. T., Sigmundsson, F. & Björnsson, H. Ice–volcano interaction of the 1996 Gjálp subglacial eruption, Vatnajökull, Iceland. *Nature* **389**, 954–957 (1997).
86. Searle, R. C. et al. The Reykjanes Ridge: structure and tectonics of a hot-spot-influenced, slow-spreading ridge, from multibeam bathymetry, gravity and magnetic investigations. *Earth Planet. Sci. Lett.* **160**, 463–478 (1998).

87. Martinez, F., Hey, R. & Höskuldsson, Á Reykjanes Ridge evolution: Effects of plate kinematics, small-scale upper mantle convection and a regional mantle gradient. *Earth-Sci. Rev.* **206**, 102956 (2020).
 88. Hess, H. H. Drowned ancient islands of the Pacific Basin. *Eos Trans. Am. Geophys. Union* **27**, 875–875 (1946).
 89. Mitchell, N. C., Stretch, R., Oppenheimer, C., Kay, D. & Beier, C. Cone morphologies associated with shallow marine eruptions: east Pico Island, Azores. *Bull. Volcanol.* **74**, 2289–2301 (2012).
 90. Kokelaar, B. P. & Durant, G. P. The submarine eruption and erosion of Surtla (Surtsey), Iceland. *J. Volcanol. Geotherm. Res.* **19**, 239–246 (1983).
 91. Sigurgeirsson, M. Á. Yngra–Stampagosid a Reykjanesi. The Younger–Stampar eruption at Reykjanes, SW-Iceland.) *Náttúrufræðingurinn* **64**, 211–230 (1995).
 92. Magnúsdóttir, A. Ö. *Characteristics of the CE 1226 Medieval Tephra Layer from the Reykjanes Volcanic System*. Doctoral dissertation. (Faculty of Earth Sciences, School of Engineering and Natural Sciences, University of Iceland, 2015).
 93. Kleemann, K. *A Mist Connection: an Environmental History of the Laki Eruption of 1783 and its Legacy*, 387 (De Gruyter, 2023).
 94. Gudmundsson, M. T., Larsen, G., Höskuldsson, Á. & Gylfason, ÁG. Volcanic hazards in Iceland. *J.ökull.* **58**, 251–268 (2008).
 95. Clare, M. A. et al. Volcanic eruptions and the global subsea telecommunications network. *Bull. Volcanol.* **87**, 1–31 (2025).
 96. Porter, C. et al. ArcticDEM-Strips, Version 4.1. Harvard Dataverse dataset, 495 <https://doi.org/10.7910/DVN/3VDC4W> (2023).
 97. Blondel, S., Ford, J., Lockwood, A., Del Ben, A. & Camerlenghi, A. Reprocessing 2-D airgun seismic reflection data SALTFLU (salt deformation and sub-salt fluid circulation in the Algero-Balearic abyssal plain) in the Balearic promontory and the Algerian basin. *Mar. Geophys. Res.* **44**, 13 (2023).
 98. Planke, S. et al. Expedition 396 methods. in *Proc. International Ocean Discovery Program*, Vol. 396 (IODP, 2023).
 99. Ingólfsson, Ó., Norðdahl, H. & Schomacker, A. Deglaciation and Holocene glacial history of Iceland. *Dev. Quat. Sci.* **13**, 51–68 (2010).
 100. Boulton, G. S., Thors, K. & Jarvis, J. Dispersal of glacially derived sediment over part of the continental shelf of south Iceland and the geometry of the resultant sediment bodies. *Mar. Geol.* **83**, 193–223 (1988).
 101. Syvitski, J. P., Jennings, A. E. & Andrews, J. T. High-resolution seismic evidence for multiple glaciation across the southwest Iceland shelf. *Arct., Antarct., Alp. Res.* **31**, 50–57 (1999).
 102. Andrews, J. T. et al. The N and W Iceland Shelf: insights into Last Glacial Maximum ice extent and deglaciation based on acoustic stratigraphy and basal radiocarbon AMS dates. *Quat. Sci. Rev.* **19**, 619–631 (2000).
 103. Eiriksson, J., Knudsen, K. L., Hafliðason, H. & Henriksen, P. Late-glacial and Holocene palaeoceanography of the North Icelandic shelf. *J. Quat. Sci.* **15**, 23–42 (2000).
- 1559691, 1542736, 1810976, and 2129685. We thank Neil Mitchell for helpful discussions. We thank the editor, Isobel Yeo and two anonymous reviewers for their constructive and insightful comments, which greatly improved this manuscript. J.P. was funded by the German Research Foundation (Grant Hu698/27) and the Woods Hole Oceanographic Institution Postdoctoral Scholarship Program. We acknowledge financial support from the Open Access Publication Fund of Universität Hamburg.

Author contributions

Conceptualization was by J.P. and C.H. Data curation was by J.P. and C.H. Formal analysis was by J.P., C.H., D.P., F.M.Z., C.D., A.F., S.B., V.E., B.H., L.I., M.L., M.S., J.O.E., L.B., D.P.Ó., and N.A. Methodology was by J.P., C.H., D.P., F.M.Z., J.F., N.A., and J.O.E. Project administration was by D.P., N.A., and C.H. Resources were by C.H. and N.A. Visualization was by J.P., D.P., C.D., A.F., and D.O.E. Writing (draught) was by J.P. Writing (editing) was by J.P., C.H., D.P., F.M.Z., and N.A. Writing (review) was by J.P., C.H., D.P., F.M.Z., K.P., C.D., A.F., S.B., V.E., J.F., B.H., L.I., M.L., M.S., J.O.E., L.B., D.P.Ó., M.L.S., and N.A.

Funding

Open Access funding enabled and organized by Projekt DEAL.

Competing interests

The authors declare that the research was conducted in the absence of any commercial or financial relationships that could be construed as a potential conflict of interest.

Additional information

Supplementary information The online version contains supplementary material available at <https://doi.org/10.1038/s43247-025-03128-w>.

Correspondence and requests for materials should be addressed to Jonas Preine.

Peer review information *Communications Earth and Environment* thanks Isobel Yeo and the other, anonymous, reviewer(s) for their contribution to the peer review of this work. Primary Handling Editors: Joe Aslin and Carolina Ortiz Guerrero. A peer review file is available.

Reprints and permissions information is available at <http://www.nature.com/reprints>

Publisher's note Springer Nature remains neutral with regard to jurisdictional claims in published maps and institutional affiliations.

Open Access This article is licensed under a Creative Commons Attribution 4.0 International License, which permits use, sharing, adaptation, distribution and reproduction in any medium or format, as long as you give appropriate credit to the original author(s) and the source, provide a link to the Creative Commons licence, and indicate if changes were made. The images or other third party material in this article are included in the article's Creative Commons licence, unless indicated otherwise in a credit line to the material. If material is not included in the article's Creative Commons licence and your intended use is not permitted by statutory regulation or exceeds the permitted use, you will need to obtain permission directly from the copyright holder. To view a copy of this licence, visit <http://creativecommons.org/licenses/by/4.0/>.

© The Author(s) 2025

Acknowledgements

We want to thank the captain, crew, and scientific party of RV Meteor expedition M201, and especially the technician of the University of Hamburg Sven Winter. We are grateful to Schlumberger for providing VISTA seismic processing software, IHS Markit for providing KINGDOM seismic interpretation software, and Shearwater for providing an academic license of Reveal seismic processing software under an academic license to OGS. High-resolution bathymetry data was provided by the Marine and Freshwater Research Institute in Iceland. Onshore Digital Elevation Models were provided by the Polar Geospatial Center under NSF-OPP awards 1043681,